Simulations of Radiocarbon in a Coarse-Resolution World Ocean Model
1.   Steady State Prebomb Distributions

J. R. TOGGWEILER, K. DIXON, AND K. BRYAN

Geophysical Fluid Dynamics Laboratory, NOAA, Princeton University, Princeton, New Jersey

This paper presents the results of five numerical simulations of the radiocarbon distribution in the ocean using the Geophysical Fluid Dynamics Laboratory primitive equation world ocean general circulation model. The model has a 4.5° latitude by 3.75° longitude grid, 12 vertical levels, and realistic continental boundaries and bottom topography. The model is forced at the surface by observed, annually averaged temperatures, salinities, and wind stresses. There are no chemical transformations or transport of ^{14}C by biological processes in the model. Each simulation in this paper has been run out the equivalent of several thousand years to simulate the natural, steady state distribution of ^{14}C in the ocean. In a companion paper the final state of these simulations is used as the starting point for simulations of the ocean's transient uptake of bomb-produced ^{14}C. The model reproduces the mid-depth ^{14}C minimum observed in the North Pacific and the strong front near 45°S between old, deep Pacific waters and younger circumpolar waters. In the Atlantic, the model's deep ^{14}C distribution is much too strongly layered with relatively old water from the Antarctic penetrating into the northern reaches of the North Atlantic basin. Two thirds of the decay of ^{14}C between 35°S and 35°N is balanced by local ^{14}C input from the atmosphere and downward transport by vertical mixing (both diffusion and advective stirring). Only one third is balanced by transport of ^{14}C from high latitudes. A moderately small mixing coefficient of 0.3 cm^2 s^{-1} adequately parameterizes vertical diffusion in the upper kilometer. Spatial variation in gas exchange rates is found to have a negligible effect on deepwater radiocarbon values. Ventilation of the circumpolar region is organized in the model as a deep overturning cell which penetrates as much as 3500 m below the surface. While allowing the circumpolar deep water to be relatively well ventilated, the overturning cell restricts the ventilation of the deep Pacific and Indian basins to the north. This study utilizes three different realizations of the ocean circulation. One is generated by a purely prognostic model, in which only surface temperatures and salinities are restored to observed values. Two are generated by a semidiagnostic model, in which interior temperatures and salinities are restored toward observed values with a 1/50 year^{-1} time constant. The prognostic version is found to produce a clearly superior deep circulation in spite of producing interior temperatures and salinities which deviate very noticeably from observed values. The weak restoring terms in the diagnostic model suppress convection and other vertical motions, causing major disruptions in the diagnostic model's deep sea ventilation.

INTRODUCTION

In the decades ahead, scientists studying the response of the global environment to anthropogenic changes will have to rely heavily on global models of ocean circulation. The most general ocean circulation models for predictive purposes are the "primitive equation" models. In solving the primitive equations in a model, one describes the local balances of heat and salt. This allows one to simulate both the wind-driven and thermohaline (density driven) circulations as responses to the forcing by sources of heat, fresh water, and momentum at the ocean's surface.

Many important applications may be carried out using large-scale models, but we must first gain an understanding of how well they work. With regard to the surface currents, heat transport, and temperature-salinity (*T-S*) structure, it is well known that primitive equation models, run with the currently available resolution, have certain chronic deficiencies. Our purpose here is to investigate a largely untested area of model performance: the processes and rates by which the subsurface layers of the deep ocean come into contact with the surface boundary. Chemical oceanographers use the word "ventilation" in referring to these processes in toto. The use of this word invokes a useful analogy because the gaseous components of seawater, like

oxygen and CO_2, reequilibrate with the atmosphere when ventilation occurs.

The ventilation of the ocean interior occurs through many processes such as bottom water formation, deep currents, convection, wind pumping, and mixing. Unfortunately, many of these processes cannot be observed or compared with model output directly. Current meter records, for example, are dominated by small-scale, high-frequency fluctuations which are not resolved by models. The time-averaged currents, most appropriate for model comparison, are generally too slow below the surface to be measured. Oceanographers must generally infer how ventilation occurs by property distributions. Primitive equation models do predict distributions of temperature and salinity in the interior of the ocean, but these fields are less than ideal diagnostics of ventilation. Temperature and salinity are not passive tracers: together they determine the distribution of density, which itself drives part of the circulation. Distributions of temperature and salt also tell us little about rates of ventilation.

In many respects, the most useful diagnostics of the ventilation of the ocean's interior come from geochemical tracers with simple boundary conditions at the ocean's surface. The first paper in this set describes the Geophysical Fluid Dynamics Laboratory (GFDL) world ocean model's simulation of the steady state distribution of ^{14}C in the ocean. Comparison between model-predicted fields of ^{14}C in the deep sea and the observed fields yields a fairly unambig-

uous assessment of deep sea ventilation rates. The decay of ^{14}C leads to a gradual differentiation of water masses by "age" or renewal time which highlights the effect of advective renewal in deep water. The ^{14}C renewal or ventilation signal, being produced in situ, is distinct from the effect of mixing, an annoyance which plagues the utility of conventional hydrographic tracers in uncovering patterns of deepwater flow. The second paper describes model simulations of the ocean's transient uptake of nuclear bomb–produced ^{14}C during the past 3 decades. With a progression of model snapshots one can visually follow the model's upper ocean ventilation processes as surface water masses pick up the bomb ^{14}C label and penetrate the interior.

In each case, ^{14}C is introduced to the model from a well-mixed atmospheric reservoir. Compared with other tracers, the input of ^{14}C to the ocean has relatively little spatial variability. This is important because the penetration of ^{14}C into the ocean's interior will not be biased by the locality in which it occurs. The time required for isotopic equilibration of ^{14}CO$_2$ and ^{12}CO$_2$ concentrations in the mixed layer of the ocean and the atmosphere is about a decade [Broecker and Peng, 1974], in contrast to the much faster chemical equilibration times for oxygen, CO$_2$, and other gaseous tracers. The long equilibration time makes the surface ^{14}C/^{12}C ratio a useful diagnostic of interior ventilation processes. The long isotopic equilibration time also means that the pulse of bomb ^{14}C entering the ocean is not completely analogous to the fossil fuel CO$_2$ entering the ocean.

Primitive equation models of the ocean circulation were first developed almost 20 years ago [Bryan, 1969] at GFDL. The coarse-resolution model used in these experiments represents the state of the art in ocean modeling of about 10 years ago. This model is essentially the same as the ocean model in the coupled ocean-atmosphere model experiments of Manabe and Stouffer [1988]. Ocean models are currently being run with much higher resolution, but computer constraints generally limit the highly resolved ocean models to single ocean basins or else make it impractical to run these models out for the several thousand model years required to simulate the steady prebomb distribution of ^{14}C in the ocean.

Coarse-resolution primitive equation models have a chronic tendency to have either a weak thermohaline circulation or thermocline temperatures which are too warm [Bryan, 1987]. Model isotherms are often depressed by several hundred meters [Bryan, 1979]. Deep salinities tend to be too fresh unless forced to be higher by some alteration of the surface boundary conditions. To ensure smooth numerical solutions, large amounts of parameterized eddy viscosity and diffusion are needed to damp small-scale transient motions. This slows and broadens large-scale flows. Western boundary currents do not separate from the coast at the proper latitudes [Sarmiento, 1986], and a spurious upwelling is known to occur landward of the western boundary currents [Veronis, 1975].

The model used in these experiments is a simplified general circulation model which displays all the tendencies noted above. It has few of the embellishments which have been suggested to improve the temperature and salinity structure. It is forced by annually averaged winds and annually averaged mixed layer temperatures and salinities. It has no sea ice and no alterations of the surface boundary conditions to simulate the effects of sea ice formation.

Vertical mixing is parameterized by simple Fickian diffusion. The model has no special features to enhance local mixing due to wind-induced turbulence or current shear. Lateral diffusion in this model is oriented along horizontal surfaces without regard to the density structure. Our plan for a future series of papers is to build up a greatly improved coarse-resolution model by relying on ^{14}C experiments like these to evaluate the merits of added features.

The study includes five separate ^{14}C experiments in which the model's circulation and gas-exchange parameters are varied. Three of the experiments are run in the "robust diagnostic" mode, in which the predicted fields of temperature and salinity are continuously adjusted toward the observed three-dimensional fields. Sarmiento and Bryan [1982] first used the robust diagnostic technique in developing a model for North Atlantic tracer simulations. The restoring of interior values toward the observed values introduces small, but artificial, sources of heat and salt into the model in an attempt to keep the model circulation consistent with the observed density field. Two of the experiments are run in the prognostic mode, in which only the surface layer temperatures and salinities are restored toward the observed values; interior temperatures and salinities adjust to an equilibrium state. Given the tendencies of the purely prognostic models, we wanted to see if improvements in the density field might produce a better simulation of the radiocarbon distribution.

MODEL DESCRIPTION

The ocean circulation model used in this investigation is based on the primitive equation model described by Bryan [1979] and Bryan and Lewis [1979]. The model's spacing between grid points is 4.5° of latitude and 3.75° of longitude. The maximum depth is 5000 m, and there are 12 vertical layers. The bathymetry of the model is shown in Figure 1.

Bathymetric constrictions like straits and deep silled channels pose a special problem for coarse-resolution models. Viewed from above, the layout of the numerical grid is like a checkerboard. Temperature, salinity, and tracer concentrations are defined at the center of the squares. The u and v components of velocity are defined at the corner points. Coastal boundaries coincide with the edges of the squares. In order to have at least one velocity point, a channel must include a minimum of two squares. This would mean that the channel's width must be at least 9° of latitude or 7.5° of longitude. While this is a necessary condition, the levels of horizontal viscosity needed in the model to define boundary currents prevent realistic flows through such narrow channels. In order to deal with this restriction, we have altered the ocean's bathymetry in two places. The Drake Passage has been gouged out to the extent that three velocity grid points and four T-S grid points lie within the gap between South America and Antarctica in the uppermost nine layers (<2559 m). Figure 2 shows a cross section of the model configuration through the Drake Passage. Iceland has also been eliminated, and the still connecting Greenland with Europe has been deepened to a depth of 1350 m. No attempt is made to resolve the Strait of Gibraltar, and no transfers of heat, salt, or tracers take place between the Mediterranean and the Atlantic.

The primitive equation model makes use of the Boussinesq and rigid-lid approximations and the hydrostatic assumption, and it represents subgrid scale turbulent viscosity as enhanced molecular mixing. The equation of motion is
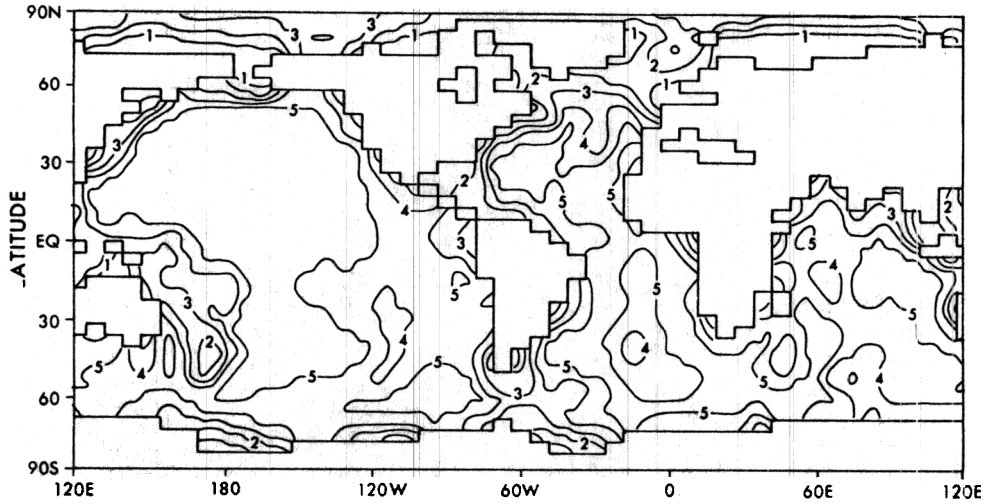
Fig.   Bottom depth distribution in the model. Contours are in kilometers.

$$\frac{\partial V}{\partial t} + V \cdot \nabla_h V + w\partial_z V + f k \times V = \frac{-1}{\rho_0} \nabla_h p$$

$$+ A_{mv}\partial_{zz}V + A_{mh}(\nabla_h^2 V + \quad (1)$$

where V is the horizontal velocity vector, w is the vertical velocity, ∇_h is the horizontal gradient operator, f is the Coriolis parameter, k is the unit vector in the vertical direction, and ρ_0 is the reference density (taken to be unity in cgs units). The hydrostatic relation gives the local pressure P at depth z as

$$P(z) = P_s + \int_z^0 g\rho \, dz \quad (2)$$

where P_s, the pressure at the ocean surface, is taken to be constant. A_{mv} represents the coefficient of turbulent mixing of momentum in the vertical, and its related term, $A_{mv}\partial_{zz}V$, represents a body force due to the mixing of momentum on a sphere. Horizontal velocities are zero at the lateral boundaries.

The equation of continuity is

$$\nabla_h \cdot V + \partial_z w = 0 \quad (3)$$

and the equation of state, $\rho = \rho(\theta, S, P)$ is approximated by a set of polynomial expressions, one for each model layer, as detailed by *Bryan and Cox* [1972].

At the upper boundary an annual mean wind stress field, $\tau(\phi, \lambda)$, interpolated from the data set of *Hellerman and Rosenstein* [1983], determines the atmosphere to ocean momentum flux.

$$A_{mv} \partial_z V = \tau \quad (4)$$

At the bottom, a slight linear drag is applied.

$$A_{mv} \partial_z V = -\alpha V \quad (5)$$

The conservation equation for salinity and potential temperature is

$$\partial_t(S, \theta) + V \cdot \nabla_h(S, \theta) + w\partial_z(S, \theta) = \partial_z[A_{hv}\partial_z(S, \theta)]$$

$$+ A_{hh}\nabla_h^2(S, \theta) + \gamma[(S^* - S), (\theta^* - \theta)] \quad (6)$$

where A_{hv} and A_{hh} are the vertical and horizontal turbulent diffusion coefficients, respectively. The γ term represents a restoring term for potential temperature and salinity to be discussed below. S^* and θ^* represent the observed salinity and potential temperature at a given grid point.

Rates of lateral mixing of momentum, defined by A_{mh}, and tracers, A_{hh}, given in Table 1, are quite large in coarse-resolution models. This is due to the requirements for smooth finite difference solutions for a given grid size. We assume, following *Bryan* [1979] and *Bryan and Lewis* [1979], that the effective lateral diffusivity for tracers is greater in the upper ocean than in the deep ocean. A_{hh} is taken to be
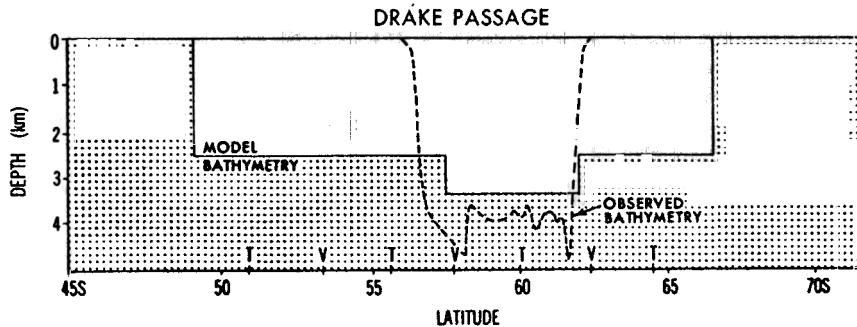

Fig. 2.   Schematic cross section of the model's representation of the Drake Passage. Tick marks labeled T and V indicate locations of tracer and velocity grid points, respectively. Observed bathymetry taken from *Whitworth et al.* [1982].

TABLE 1   Mixing and Damping Parameters Used by Prognostic, RDIAG1, and RDIAG2 Circulation Models

	Prognostic	RDIAG1	RDIAG2
A_{mv}, cm^2 s^{-1}		20	20
A_{mh}, cm^2 s^{-}		2.5×10^9	2.5×10^9
A_{hv}, cm^2 s^{-1}		0.3–1.3	1.0
A_0, cm^2 s^{-1}		0.8	1.0
C_r		1.05	0
A_{hh}, cm^2 s^{-1}		1.0–0.5×10^7	1.0–0.5×10^7
A_s, cm^2 s^{-1}		1.0×10^7	1.0×10^7
A_b, cm^2 s^{-1}		0.5×10^7	0.5×10^7
γ_s, day^{-1}		1/30	1/30
γ_d, year^{-1}		1/50	1/50

$$A_{hh} = A_b + (A_s - A_b) \exp(-z/500) \qquad (7)$$

where A_s is the surface value, A_b is the value at the maximum model depth of 5000 m, and z is expressed in meters. A parameterization which allows lateral diffusion to occur along isopycnal surfaces rather than level surfaces is not included in this basic model. No fluxes of tracers are allowed across the bottom or lateral walls. The finite difference scheme on which the model is based is given by Bryan [1969].

The model used here is run in both the prognostic and "robust diagnostic" modes. In both cases the model's surface temperatures and salinities are continuously adjusted toward the observations, using the restoring term in equation (6), in an attempt to replicate the boundary fluxes of heat and fresh water at the interface between the ocean and atmosphere. The restoring parameter γ has a value of 1/(30 days) in the uppermost layer. In the prognostic mode, γ is set to zero everywhere below the surface layer, such that water properties in the interior are entirely predicted by the model.

In the robust diagnostic mode we have set γ equal to 1/(50 years) below the surface layer, such that the model's interior temperatures and salinities are pushed gently toward observations everywhere in the model domain. The interior restoring introduces small, but artificial, sources of heat and salt into the model. Because of the restoring term, the diagnostic version of the model does not depend on slow mixing processes to reach steady state and is computationally less expensive than the prognostic model.

The observed potential temperatures and salinities used in the restoring terms in equation (6) have been interpolated from the annually averaged data sets of Levitus [1982]. The values of S^* and T^* used for restoring the model's upper layer represent an average of the upper 50 m. Averaging over the upper 50 m tends to reduce the impact of thin, seasonal meltwater layers with very low salinities which appear in the upper layers of the Levitus data set in some high-latitude areas.

Three separate realizations of the ocean circulation have been computed, one using the prognostic model and two with the diagnostic model, to produce five different ^{14}C simulations. The greater number of ^{14}C simulations reflects multiple ^{14}C runs using the same circulation with different treatments of gas exchange. Input of ^{14}C to the ocean via gas exchange will be discussed in the next section.

Two integrations of the robust diagnostic circulation, which we will call RDIAG1 and RDIAG2, were carried out using two different values of the vertical diffusion coefficient for heat, salt, and tracers, A_{hv}. In both the prognostic

integration and RDIAG1, the diffusion coefficient increases with depth from 0.3 cm^2 s^{-1} in the upper kilometer to 1.3 cm^2 s^{-1} in the deepest layer, following the approach of Bryan and Lewis [1979]. The vertical diffusion coefficient is calculated according to the formula

$$A_{hv} = A_0 + \frac{C_r}{\pi} \tan^{-1} [4.5 \times 10^{-3}(z - 2.5 \times 10^3)] \qquad (8)$$

where z is the depth in meters. The vertical diffusion coefficient at 2.5 km is given by A_0, and the range between the top and bottom is given by C_r.

The vertical diffusion coefficient in RDIAG2 is set equal to 1.0 cm^2 s^{-1} everywhere in the model domain. Experiment specifications for damping and diffusion parameters are listed in Table 1.

Each robust diagnostic integration of the temperature, salinity, and velocity fields reached equilibrium within 300 years. The circulation models were run out for an additional 450 years while V was sampled every 5 years to produce average flow fields for the ^{14}C integrations. Three ^{14}C integrations were run out for the model equivalent of 2000 years using time-mean velocity and convection fields from the robust diagnostic calculations.

The model continuously checks for unstable vertical density gradients. When instabilities occur, the convective mixing parameterization is activated and the unstable parts of the water column are completely mixed, so that the temperature, salinity, and ^{14}C are conserved. For the robust diagnostic models, the frequency of convection is sampled every time step and averaged over years 700–750 in order to produce a three-dimensional field of convection occurrence for the ^{14}C tracer calculations.

In the prognostic calculation we performed two ^{14}C simulations concurrently with the temperature, salinity, and velocity components. The full prognostic model was run out for 3500 years. The technique of Bryan [1984] was used to accelerate the approach to equilibrium in the deep water in all five experiments.

The observed global averages for potential temperature and salinity at the midpoint of each model level are shown in Table 2 along with the global averages from the prognostic model. Bottom water temperatures in the model are in good agreement with the observations, but bottom salinities are about 0.25‰ too fresh. The temperature differences between the model and the observations are largest between levels 4 and 7 (295–1131 m), reaching maximum deviations of about 4°C. There is no minimum in salinity in the prognostic model's global mean profile. The salinity minimum in the

TABLE 2. Global Mean Potential Temperatures and Salinities at Model Layer Depths for Prognostic model and observations

Model Layer	Depth of Layer, m		Mean θ^*, °C	Prognostic, θ °C	Mean S^*, ‰	Prognostic S, ‰
	Midpoint	Bottom				
1			17.65	17.66	34.75	34.75
2			15.52	16.39	34.96	34.91
3			12.59	14.79	35.00	34.95
4			9.88	13.01	34.88	34.915
5			7.44	11.19	34.71	34.85
6			5.35	9.27	34.63	34.785
7			3.76	7.20	34.65	34.76
8			2.71	5.21	34.72	34.75
9			1.97	3.22	34.73	34.67
10			1.53	2.07	34.74	34.615
11			1.15	1.32	34.73	34.58
12			0.92	0.97	34.73	34.57
Average			3.49	5.16	34.73	34.70

Average is volume weighted.

observed global mean profile occurs in layer 6 (755 m), the depth where the temperature deviation from observations is largest.

Table 3 shows the layer by layer temperature and salinity deviations of the robust diagnostic integrations, RDIAG1 and RDIAG2, from the observed means. Maximum deviations are found at model levels 4 (295 m) and 5 (483 m) where the predicted temperatures are 2°-3°C warmer than the observations. The deviations for RDIAG2 (A_{h_v} = 1.0 cm² s⁻¹) are 50% larger than those for RDIAG1. Because RDIAG1 and the prognostic integration use the same vertical mixing formulation, one can directly compare the thermocline temperature deviations in the two models and gain an appreciation for the strength of the restoring terms in the robust diagnostic models. The restoring term in RDIAG1 basically cuts the prognostic model's 3.8°C temperature excess at 483 m (level 5) in half. Temperature and salinity deviations diminish at depth in the robust diagnostic models because the 1/(50 year) restoring time constant is much more effective at depth where heat and salt transports are small.

ADDING ¹⁴C TO THE MODELS

The ¹⁴C content in a sample of wood, sediment, or ocean water is usually expressed as the deviation of the ¹⁴C/¹²C ratio in parts per thousand from a standard ratio. This notation is referred to as Δ¹⁴C. The isotopic standard chosen in the early days of the radiocarbon era was taken to be the ¹⁴C/¹²C ratio in the nineteenth-century tree rings. This standard was selected as an approximation of the ¹⁴C/¹²C ratio in the pre-industrial atmosphere. Carbon 14 atoms make up about one part in 10¹² of the carbon pool in the atmosphere, ocean, and biosphere.

In running the model, we use an arbitrary scale to express the ¹⁴C/¹²C ratio. We fix the atmospheric composition for the model at 100 units. The average ¹⁴C/¹²C ratio for the ocean is about 15% depleted (−150‰) with respect to the pre-industrial atmosphere. The model integrations therefore begin with a homogeneous ocean containing a ¹⁴C "concentration" of 85 units. Carbon 14 has a half-life of 5730 years. At each ocean grid box the ¹⁴C concentration is reduced by the product of the ¹⁴C decay constant, 1.2097×10^{-4} yr⁻¹, and the box concentration to simulate radiocarbon decay. When presenting the model results, we convert our arbitrary model units into the standard Δ¹⁴C notation as follows:

$$\Delta^{14}C \text{ (reported units)} = (\text{model units} - 100) 10 \quad (9)$$

Δ¹⁴C is a ratio and not a concentration. Because we do not include the chemical transformations of ¹⁴CO₂ and ¹²CO₂ in the model, there is no distinction between the model's units and a simple concentration. We will use the term "¹⁴C

TABLE 3. Globally Averaged Deviations of Temperature and Salinity for RDIAG1 and RDIAG2 From Observations at Model Layer Depths

Model Layer	$(\theta - \theta^*)$, °C		$(S - S^*)$, ‰	
	RDIAG1	RDIAG2	RDIAG1	RDIAG2
	−0.06	−0.11	−0.002	−0.002
	0.68	0.95	−0.054	−0.121
	1.77	2.37	−0.041	−0.098
	2.21	3.02	0.052	0.017
	1.97	2.92	0.116	0.121
	1.28	2.24	0.086	0.122
	0.64	1.37	0.024	0.051
	0.26	0.69	<0.001	0.003
	0.13	0.36	0.007	0.003
	.10	0.18	0.005	0.004
	0.10	0.11	0.004	0.003
	−0.01	−0.03	−0.005	−0.006

TABLE 4. Summary of ^{14}C Model Experiments

Experiment	Flow Field	Vertical Diffusion, cm^2 s^{-1}	Gas Exchange, mol C m^{-2} yr^{-1}
	RDIAG1	0.3–1.3	20
	RDIAG1	0.3–1.3	wind speed dependent
	RDIAG2	1.0	wind speed dependent
	prognostic	0.3–1.3	wind speed dependent
	prognostic	0.3–1.3	(same wind speed dependence as B, C, and P) × 1.2

concentration" freely in the text as a substitution for the potentially more confusing "^{14}C/^{12}C ratio."

We have combined the three flow fields (RDIAG1, RDIAG2, and the prognostic run) with different treatments of gas exchange to produce five ^{14}C experiments (Table 4). In experiment A we use the flow field from RDIAG1 (variable A_{hv}) and a gas exchange formulation in which the gas exchange rate is a constant, equivalent to 20 mol C m^2 yr^{-1}, at all grid points. If we assume there are 2 mol C m^{-3} in typical ocean surface water, the rate μ at which the surface water ^{14}C content is changed by contact with the atmosphere is given by the expression

$$\mu = \frac{20 \text{ mol m}^{-2} \text{ yr}}{2 \text{ mol m}^{-3} \times DZ_1 \, 365 \text{ days yr}^{-1}} \quad (10)$$

where DZ_1 is the depth of the surface box and μ is given in reciprocal days.

In experiment B we use the flow field from RDIAG1 and a gas exchange formulation in which the CO$_2$ exchange rate is proportional to wind speed following Broecker et al. [1985a]. The exchange rate μ is given in this case by the expression

$$\mu = \frac{[3.5 \times (\text{wind speed} - 2)] \text{ mol m}^{-2} \text{ yr}^{-1}}{2.0 \text{ mol m}^{-3} \times DZ_1 \times 365 \text{ days yr}^{-1}} \quad (11)$$

where wind speed is measured in meters per second. Monthly mean wind speed data over open water have been interpolated from Esbensen and Kushnir [1981] onto the model grid. Monthly gas exchange rates were computed and averaged over the year, assuming zero exchange rates for

months and grid boxes where the ocean is ice covered [Alexander and Mobley, 1976]. Figure 3 shows a map of the annual average gas exchange rate in moles C per square meter per year calculated by expression (11). The globally averaged gas exchange rate computed by expression (11) and Esbensen and Kushnir's wind speed data is equivalent to 16.6 moles C/m^{2}yr.

In experiment C we use the wind speed dependent gas exchange formulation of experiment B and the flow field from RDIAG2 ($A_{hv} = 1.0$ cm^2 s^{-1}).

The two prognostic experiments, P and P', both use wind speed dependent gas exchange rates. Experiment P uses the same gas exchange rates used by B and C and illustrated in Figure 3. Experiment P' uses the gas exchange rates used by experiment P multiplied by 1.20. The global mean gas exchange rate for P' is thus approximately 20 mol C m^{-2} yr^{-1}. Box model experiments [Oeschger et al., 1975] suggest that 20 mol C m^{-2} yr^{-1} is a much more appropriate global mean gas exchange rate than the 16.6 mol C m^{-2} yr^{-1} value we compute from Broecker et al.'s formula and Esbensen and Kushnir's wind speed data.

In addition to the transport of ^{14}C by ocean currents, ^{14}C is also transported through the ocean as particulate matter produced by marine organisms. The transport of biogenic material from the upper ocean causes CO$_2$ concentrations to be higher in deep water than in surface water. We do not include this effect in the model. When ^{14}C is used as a tracer, it is the ratio of ^{14}C to ^{12}C in a water sample that is of interest. Both ^{14}C and ^{12}C are fixed into biogenic particles in the same ratio in which they are found in surface water.
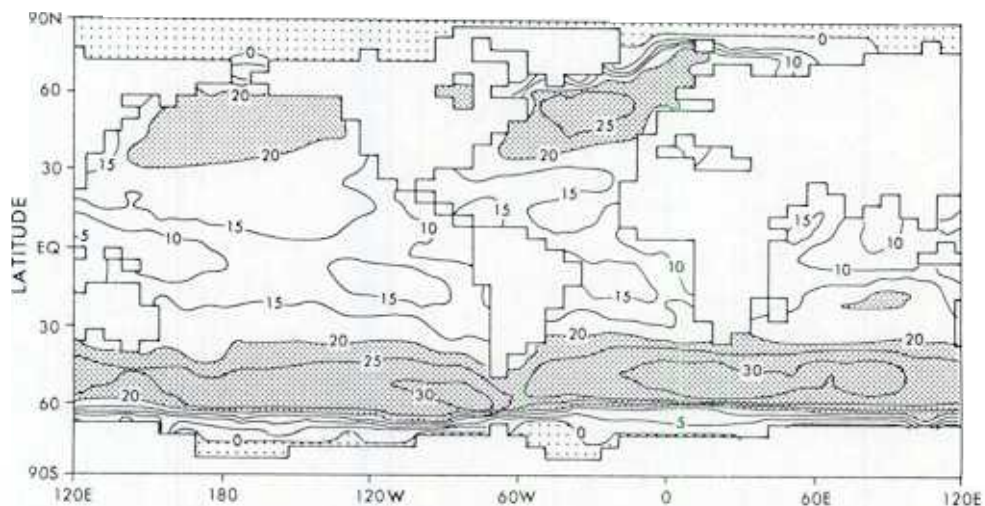

Fig. 3. Spatial distribution of wind speed dependent gas exchange rates (in moles CO$_2$ per square meter per year) used in the B, C, and P experiments. Areas with dense stippling have gas exchange rates in excess of 20 mol CO$_2$ m^{-2} yr^{-1}. In areas with light stippling the gas exchange has been set to zero because of year-round sea ice cover.

When these particles are metabolized in the deep sea, both ^{12}C and ^{14}C concentrations are increased. Therefore the effect of biological transport on the $^{14}C/^{12}C$ ratio is much smaller than the effect of biological transport on the ^{14}C or ^{12}C concentrations themselves. Any error introduced by ignoring the biological transport of carbon is less than 10% of the signal produced by the circulation and decay [Fiadeiro, 1982].

Because our radiocarbon simulations do not predict gas transfer on the basis of actual $^{12}CO_2$ and $^{14}CO_2$ gradients at the surface, we do not to include the effect of isotopic fractionation between gaseous and dissolved CO_2 phases. In the present application the effect of isotopic fractionation is not significant. When $^{14}C/^{12}C$ ratios measured in surface seawater and atmospheric CO_2 are converted to the standard $\Delta^{14}C$ notation, a correction is made to reflect $^{13}C/^{12}C$ differences between seawater and atmospheric CO_2 [Stuiver and Polach, 1977]. The effect of isotopic fractionation during gas exchange is almost completely accounted for by this correction. Our model results, without isotopic fractionation, are directly comparable to observed data which are reported using the Δ convention.

MODEL CIRCULATION

The mode of ocean circulation of most importance for ventilating the deep sea is the vertical overturning. This mode of circulation and ventilation is the most difficult to observe in the real ocean but is easily differentiated by radiocarbon. The overturning for the prognostic and RDIAG1 models, illustrated as zonally integrated meridional transport stream functions, is shown in Figures 4a and 4b, respectively. In the diagrams in Figure 4 the total transports of all the ocean basins are shown in one section. Figure 5 shows the overturning of the prognostic model broken down among the Atlantic, Pacific, and Indian ocean basins.

The overturning in the ocean is usually thought of as a manifestation of the thermohaline circulation. In the upper ocean, however, the downward pumping and upwelling induced by the wind stress plays a dominant role. Two shallow overturning cells straddle the equator in Figures 4a and 4b which are driven by the divergence of the Ekman transport under the trade winds. The Ekman transport away from the equator at the surface is compensated by inflow toward the equator above 400 m depth. Nearly all the equatorial overturning in Figures 4a and 4b is accounted for in the Pacific basin (Figure 5). This is due primarily to the fact that surface stresses under the trade winds in the Atlantic and Indian oceans are highly seasonal and as such are greatly reduced in the annual mean wind stress field. In the vicinity of the westerlies near 40° latitude in both hemispheres, the Ekman transport is toward the equator. The convergence of the two surface transport regimes results in downwelling throughout the subtropics.

The downwelling in mid-latitudes is also linked with wind-driven divergences in the subpolar regions to produce another set of overturning cells. Here there are marked asymmetries between hemispheres and notable differences between the prognostic and diagnostic models. The overturning cell in the northern hemisphere is much weaker and shallower than the corresponding cell in the southern hemisphere. One reason for the relative weakness of the northern cell stems from the thermohaline circulation in the North Atlantic which counters the Ekman-induced cell. The ex-

traordinary depth to which the subpolar cell extends in the southern hemisphere (~ 3500 m) is due to the presence of the Drake Passage and its effect on the local geostrophic balance. Much more will be said about this feature in the Discussion section. The vertical penetration of the downward flow joining the southern equatorial and subpolar cells is deeper and more vigorous in the prognostic model than in the diagnostic model.

Between 1000 m and 2500 m the meridional overturning in the model is dominated by a flow of deep water from the northern to the southern hemisphere, compensated by a return flow of thermocline water above 1000 m. This counterclockwise cell is entirely due to the overturning circulation of the North Atlantic (Figure 5). The southward flow of this circulation represents the flow of North Atlantic Deep Water (NADW). One can anticipate a major problem with the model ^{14}C simulations by noting that virtually all of the southward flow in both models' NADW is above 2500 m, while in observations much of the flow is found well below 2500 m. The overturning related to the formation of NADW is about 50% more vigorous in the prognostic model than the corresponding overturning in RDIAG1.

Near the bottom there is a northward flow of abyssal water from the southern hemisphere to the north, compensated by a return flow above 3500 m depth. The deep inflow at the bottom corresponds to Antarctic Bottom Water (AABW). The AABW flows northward into all three ocean basins but most strongly in the Pacific. The flow of bottom water from the south is about one third more vigorous in the prognostic model.

Since direct measurements of the time-mean meridional overturning of the ocean are impossible to make, it is very difficult to make a quantitative verification of the model circulation. There are a few locations for which indirect estimates are available, however. The flows of deep and mid-depth water in the South Pacific have been calculated by inverse methods from the "Scorpio" expedition (USNS Eltanin cruises 28 and 29, 1987) data by Wunsch et al. [1983]. They found a pattern of northward bottom water flow, southward return flow at mid depths, and an equatorward flow of intermediate water much like that illustrated in Figure 5c. The observed flux of bottom water was 9-12 Sv compared with the 6.5-Sv flow in RDIAG1 and the 9.1-Sv flow in the prognostic model. The total southward transport of NADW at 24°N has been estimated by Roemmich and Wunsch [1985] to be approximately 20 Sv. This is 8 Sv higher than the maximum transport predicted by RDIAG1 and about the same as the transport in the prognostic model.

So far only the zonally integrated overturning has been considered. The vertical velocities at the base of layer 1 (51 m) have been mapped in Figure 6 for the prognostic model. Because the spatial pattern of vertical velocity near the surface is dominated by the wind forcing, the layer 1 vertical velocity pattern for the diagnostic models is essentially the same as that illustrated for the prognostic model.

Ekman suction induces intense upwelling in the equatorial regions of the Pacific and Atlantic basins. The center of the zone of most intense upwelling in the equatorial Pacific is located near 150°W. This result is consistent with the predictions of a much more detailed equatorial Pacific model [Philander et al., 1987]. Maximum rates are 230 m yr^{-1} in the Pacific and 150 m yr^{-1} in the Atlantic. The Indian Ocean appears anomalous because the seasonal monsoon wind
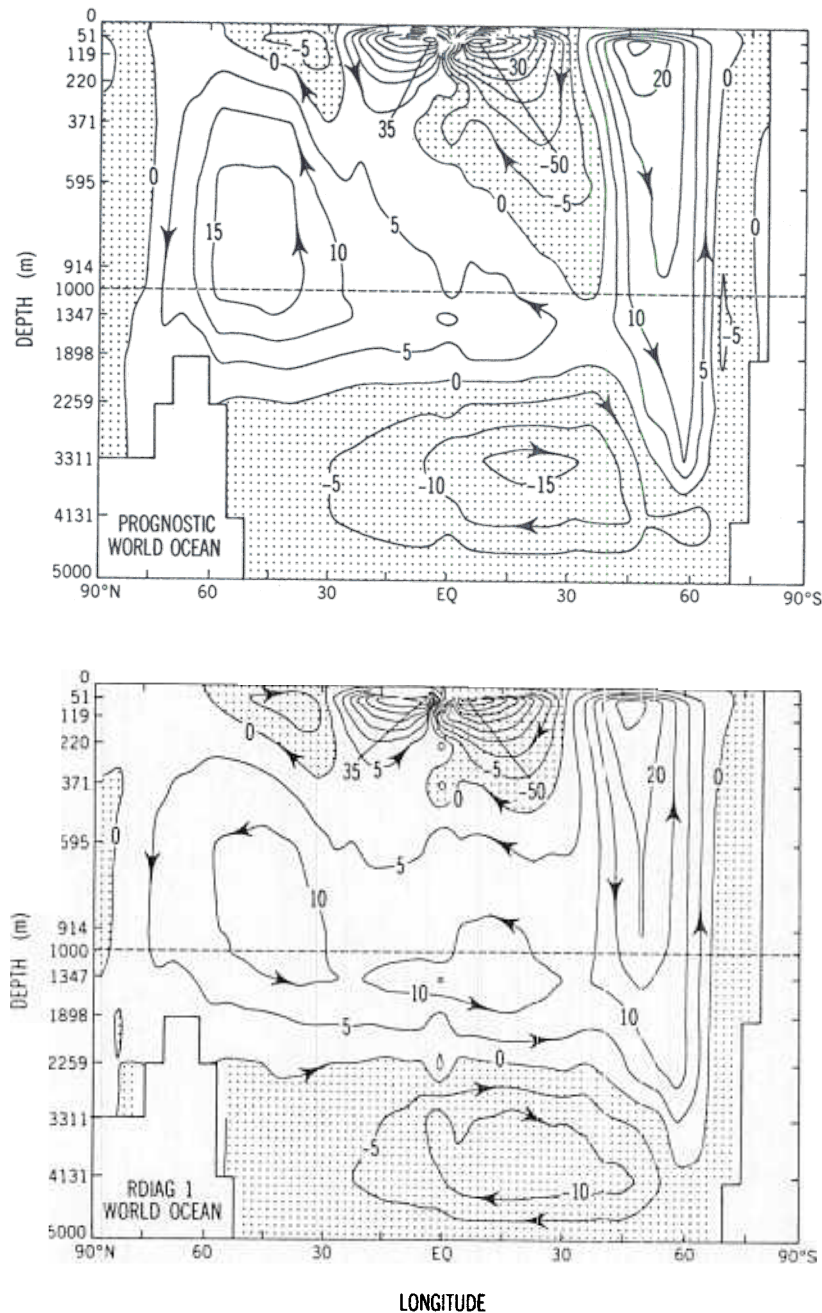
Fig. 4.   Transport stream function of the zonally integrated overturning in the vertical-meridional plane (in units of megatons per second or sverdrups) corresponding to the (top) prognostic and (bottom) RDIAG1 flow fields. The vertical scale for the upper kilometer has been expanded.

stresses are almost completely cancelled out in the annual mean. The strong upwelling at the equator is balanced by a diffuse downwelling in the adjacent subtropical gyres where downward velocities are typically 30 m yr^{-1}.

One of the most prominent features in Figure 4 was the deep overturning cell in the circumpolar zone of the southern hemisphere. The upper branch of this cell consists of equatorward Ekman transport driven by the very strong westerly winds in the southern ocean. Figure 6 hints that the downward motions in the circumpolar overturning cell are discontinuous and most intense in a few places, particularly off the tip of South America and off the southwest coast of Australia. Examination of the vertical velocity maps at each of the model layers bears this out. The wind stress south of the

maximum westerlies generally produces widespread upwelling. Figure 6 gives some indication that the upward velocities are even more localized than the downward motions. Strong localization of the upwelling is indeed evident at the deeper levels but is probably not realistic. The model stratification is very weak near Antarctica, more so than in the real ocean. Deflections of model currents around deep topographic features allow large vertical motions to occur which probably do not have counterparts in the real ocean.

The convective overturning of unstable water parcels also contributes to the vertical penetration of surface water mass properties in the model. Figure 7 shows the frequency of convection occurrence in the prognostic model between levels 1 and 2 (51 m). Near the surface, convection appears
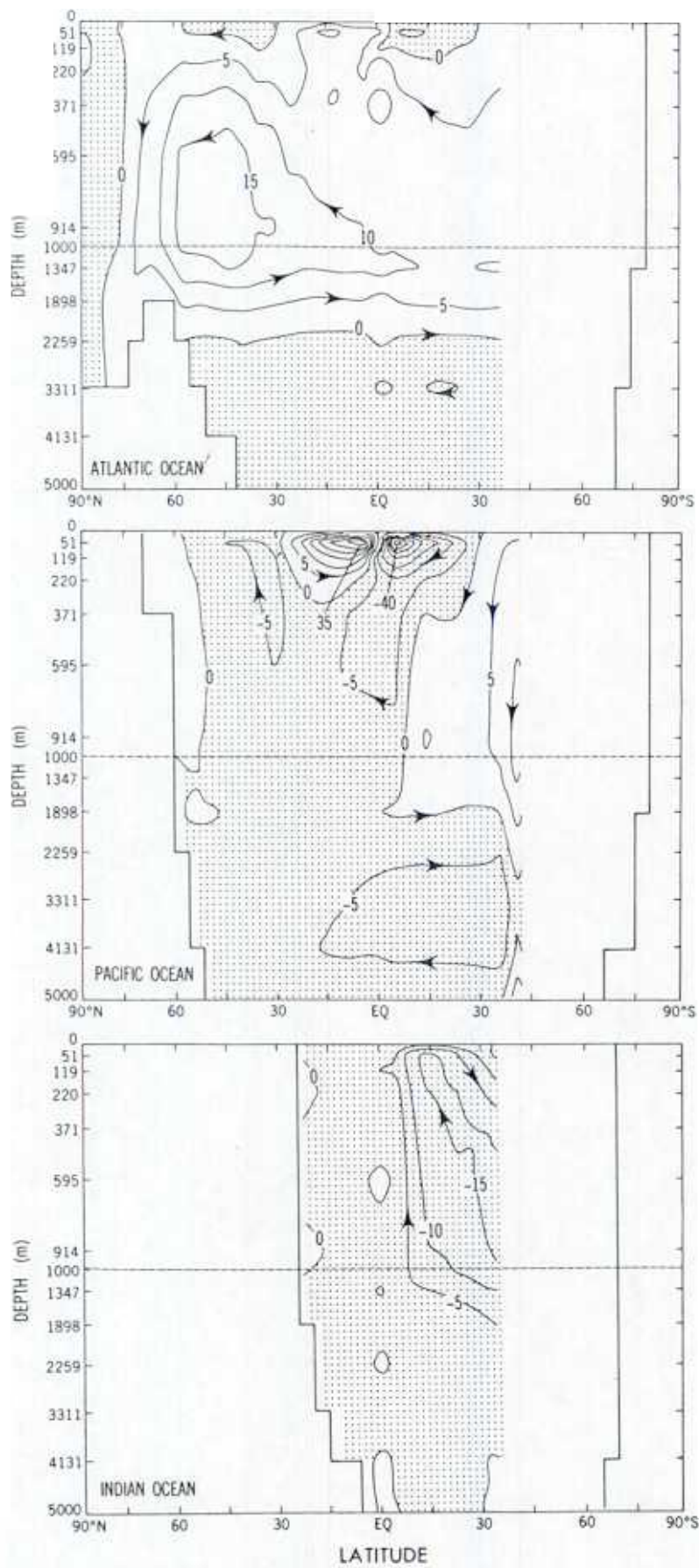
Fig. 5. Breakdown of the total meridional overturning of the prognostic model (Figure 4a) among the Atlantic, Pacific and Indian ocean basins.
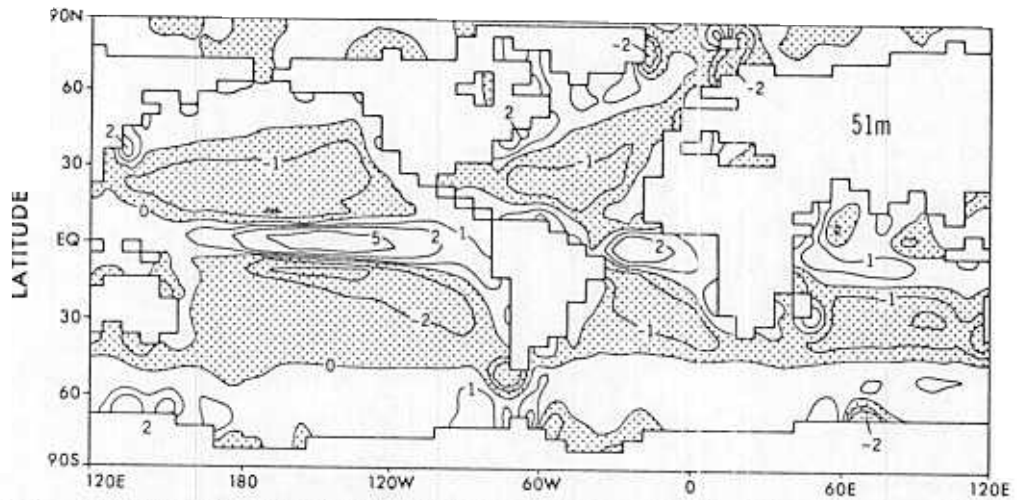
Fig. 6. Spatial distributions of vertical velocity (in units of 10^{-4} cm s^{-1}) at 51 m in the prognostic model. Contours have been smoothed using a nine-point smoothing function. In the stippled areas, vertical motions are downward. Contours are drawn at 0, 1, 2, and 5×10^{-4} cm s^{-1}.

to be aligned with the major mid-latitude currents which separate the subtropical and subpolar gyres. These areas coincide with the transition from net buoyancy gain at the surface to net buoyancy loss. Convection is very extensive in the North Atlantic and extends from the Gulf Stream up into the Norwegian Sea. Areas in which convection penetrates to deeper levels coincide with well-known areas of deep water formation [*Warren*, 1981] in the Norwegian-Greenland Sea, the Labrador Sea, and the Weddell Sea. Areas of convection between 35°S and 45°S coincide with regions of downwelling in Figure 6. Convection in this latitude band is related to formation of the "Subantarctic Mode Water" described by *McCartney* [1982]. This type of convection occurs in both the Indian and Pacific oceans within the zone of convergent Ekman transport. It is tagged with large amounts of bomb ^{14}C and will be dealt with more fully in part 2 [*Toggweiler et al.*, this issue].

Other model circulation diagnostics of interest include a northward heat transport at 25°N of 0.98×10^{15} W, which is very similar to the model results of *Bryan and Lewis* [1979].

Maximum transport in the Gulf Stream is about 40 Sv, about equal to that observed at 30°N, upstream of the recirculation region [*Knauss*, 1969]. The flow through the Drake Passage in the prognostic model is about 195 Sv, which is much stronger than the 130 ± 20 observed by *Whitworth and Peterson* [1985]. One of the simplifications made in setting up this model dictates that there be no net flow around Australia. About 15 Sv of model water flows southward through the Indonesian Straits from the Pacific to the Indian Ocean in the upper 300 m. This is compensated by 15 Sv of flow in the opposite direction at deeper levels. The upper level flow is consistent with the highest estimates for southward flow through the Indonesian Straits [*Piola and Gordon*, 1984] but is 3 times larger than more conservative estimates [see *Fine*, 1985].

RESULTS

Globally Averaged Profiles

The presentation of ^{14}C results begins with globally averaged vertical profiles in Figures 8a and 8b, which allow a
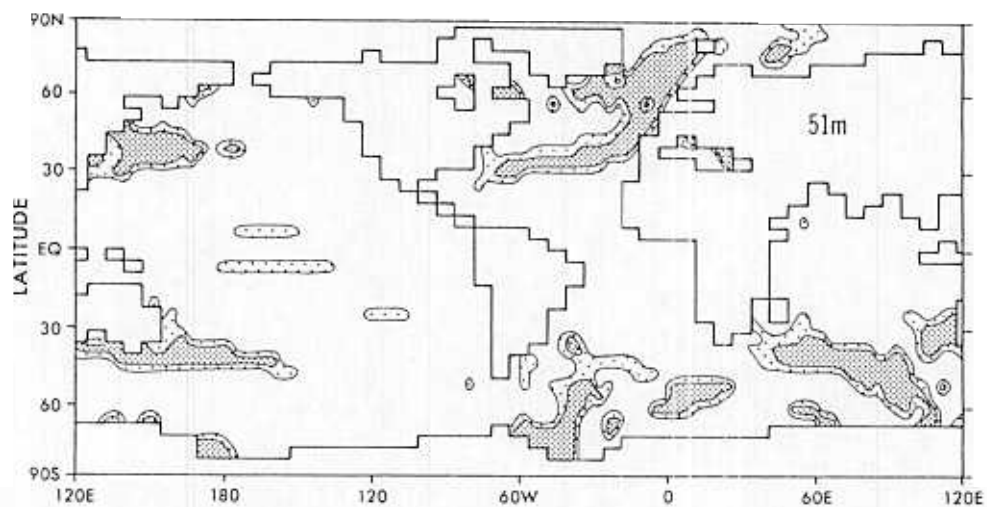

Fig. 7. Intensity of convection at 51 m in the prognostic model. Dense stippling indicates that convection occurs between layers more than 75% of the time. Light stippling indicates that convection occurs more than 25% and less than 75% of the time.
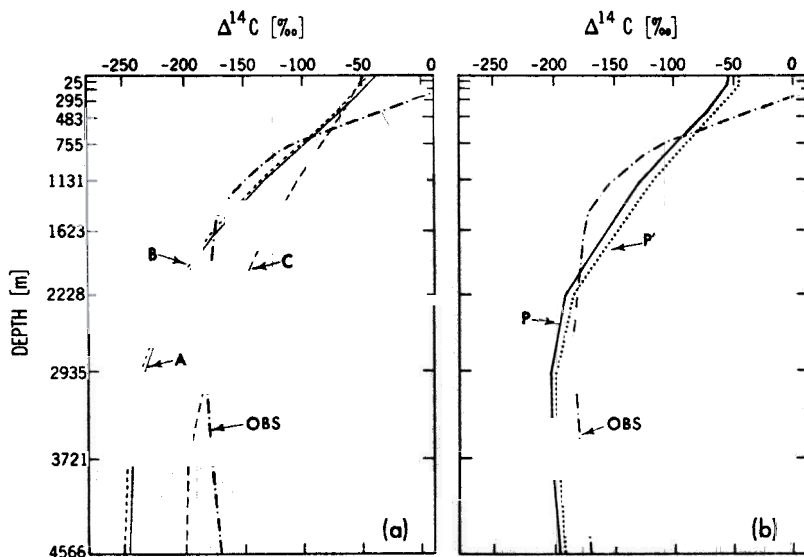
Fig. 8. Globally averaged vertical profiles of $\Delta^{14}C$ (per mil) corresponding to (a) the GEOSECS observations and experiments A, B, and C and to (b) the observations and experiments P and P'. Consult Table 4 for a summary of model experiments.

comparison of the robust diagnostic runs A, B, and C and the prognostic model runs P and P' with the Geochemical Ocean Sections Study (GEOSECS) observations. The observed profile is taken from data of *Stuiver and Ostlund* [1980, 1983] and *Ostlund and Stuiver* [1980] and includes bomb ^{14}C in the upper 750 m. All three of the robust diagnostic runs have their oldest (most negative) ^{14}C concentrations at the bottom, whereas the prognostic models and the observations have midwater minima. The observations are distinctly older between 750 m and 1500 m than any of the model simulations. This is the depth range associated with the largest temperature and salinity anomalies in the prognostic model.

Experiment C, using a uniform 1.0 cm^2 s^{-1} vertical diffusion coefficient, has much younger water throughout the water column than experiments A and B, which have 0.3 cm^2 s^{-1} vertical diffusion in the upper kilometer. Vertical mixing thus appears to have a major impact on deepwater values. The prognostic experiments use the same vertical mixing as A and B but have much younger values near the bottom. The prognostic models are clearly superior in producing the best average fit to the observations.

Figure 8b shows that the 20% higher gas exchange rates in experiment P' increase global mean ^{14}C values in deep water by about 7.5‰ compared with P. The globally averaged ^{14}C profiles for the A and B runs are even more similar. The A simulation uses a spatially uniform gas exchange rate, while the B simulation uses a wind speed dependence to determine local exchange rates; in all other respects these models are identical. In high latitudes the wind speed dependent rates are as much as 50% higher than the uniform rate in experiment A, and in low latitudes they are half the uniform rate. One conclusion we can draw from the global average profiles in Figure 8 is that the spatial dependence of gas exchange is a second-order effect for deepwater ^{14}C, i.e., a 20% difference in global average rates has a greater impact than the 100% differences in geographic distribution.

This conclusion can be understood in terms of basic properties governing ^{14}C concentrations in the ocean. First, the main rate-limiting step governing the penetration of ^{14}C into the deep sea is mixing through the thermocline. (We

offer this assertion without support but will illustrate it more fully later in the paper.) Second, the long 10-year equilibration time for exchanging carbon isotopes between the air and ocean surface layer allows homogenization of upper ocean ^{14}C differences resulting from spatially varying gas exchange rates. The penetration of ^{14}C through the thermocline is thus not influenced very much by geographic differences in gas exchange rates.

Prebomb Surface Water

Figure 9 shows a map of the predicted prebomb surface distribution of ^{14}C for experiments P, B, and C. Areas with a ^{14}C content higher than −30‰ (3% depleted relative to the pre-industrial atmosphere) are shown with heavy stippling, while areas with a ^{14}C content lower than −100‰ are shown with light stippling.

A steady state between air and ocean surface ^{14}C concentrations has not been achieved at any time during this century. Prior to the introduction of ^{14}C produced by nuclear weapons testing, the atmosphere's $\Delta^{14}C$ had been lowered owing to the industrial release of fossil CO_2 to the atmosphere which contained no ^{14}C (the "Suess effect"). The output of industrial CO_2 began in earnest in the late nineteenth century, so that one must go to ^{14}C records in banded corals to recover observations which can be compared with the model's output. Table 5 shows a compilation of coral records from eight sites in the Atlantic and Pacific oceans. In some cases the coral records contain complete histories back to the 1800s which document the fossil fuel dilution in the ocean. In other cases the coral records go back to the early 1950s and the Suess effect has been estimated. In addition to anthropogenic disturbances the atmosphere's ^{14}C content has varied naturally. *Druffel and Suess* [1983] have summarized tree ring measurements which show that the atmosphere's $\Delta^{14}C$ in the last half of the nineteenth century was −6‰. Table 5 lists the reconstructed ocean-atmosphere ^{14}C differences for the eight coral sites which can be compared with the model predictions in Figure 9.

These few observations show that the average pre-industrial ocean-atmosphere difference was about −40‰ for
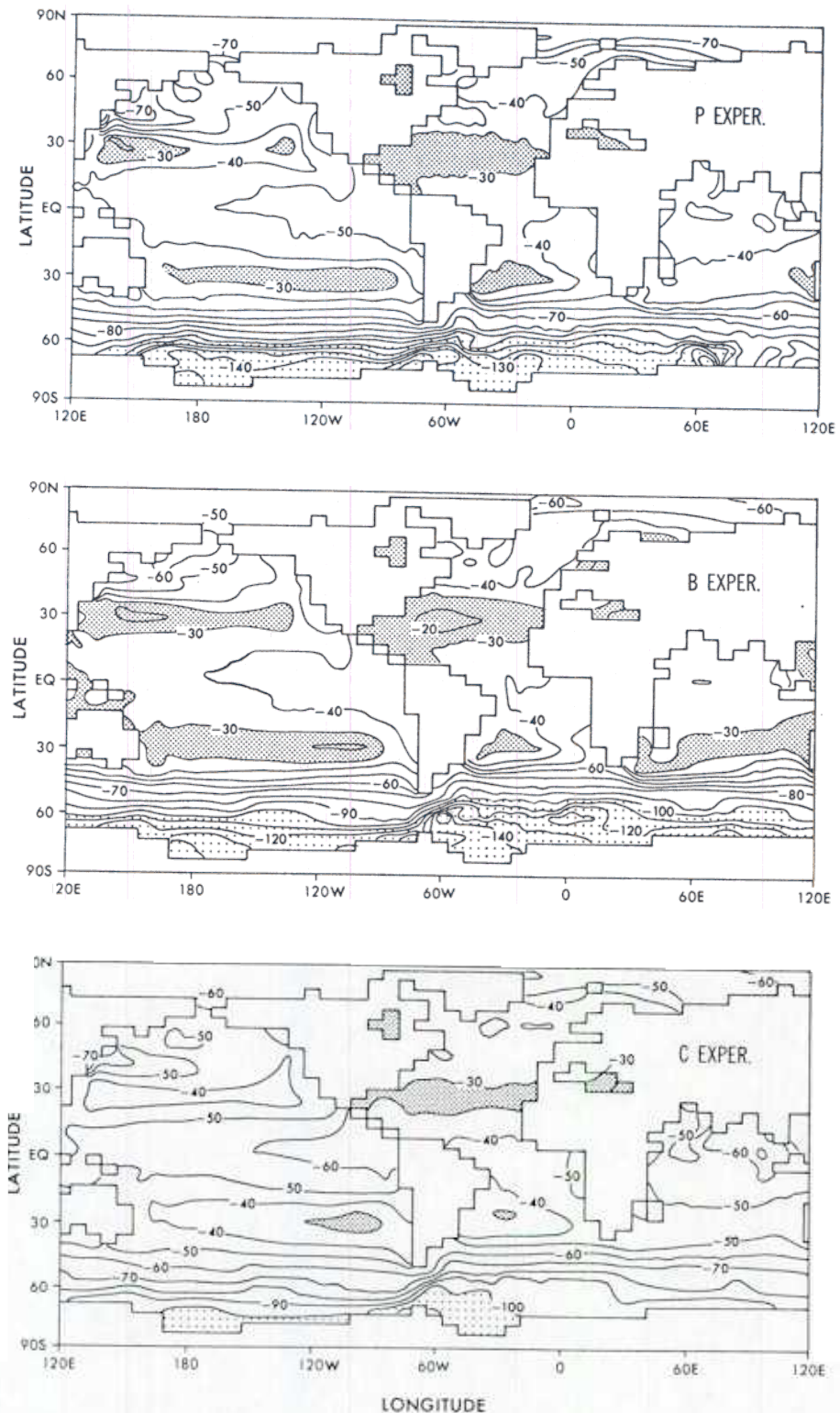
Fig. 9. Spatial distribution of $\Delta^{14}C$ (per mil) in the surface layer predicted for steady state prebomb conditions: (top) experiment P, (middle) experiment B, (bottom) experiment C.

the low- and middle-latitude regions where corals grow. The smallest differences are found at Okinawa (−23) and Bermuda (−22), and the largest are found in the eastern equatorial Pacific at the Galapagos Islands (−60). On average, the P model results (−39) are in good agreement with the observations. The B experiment's surface values are systematically higher than those of P.

Both the P and B models predict very low surface values around Antarctica. *Broecker and Peng* [1982] summarize prebomb seawater ^{14}C measurements from the mid-1950s. Their high-latitude values should be only weakly affected by industrial CO_2 and bomb ^{14}C from the early tests. These observations show high-latitude surface waters in the southern hemisphere dipping below −100‰.

TABLE 5. Pre-1900 Values of $\Delta^{14}C$ in Surface Water as Recorded by Banded Corals

Site	Prebomb	Ocean Suess Effect*	Pre-1900†	Pre-1900 Ocean-Atmosphere Difference‡	Predicted§	Reference
Fiji	−60	(−12)	(−48)	−42	−39	*Toggweiler* [1983]
Galapagos	−72	− 6	−66	−60	−53	*Druffel* [1981]
Fanning	−59	(−10)	(−49)	−43	−52	*Druffel* [1987]
Panama	−58	(−10)	(−48)	−42	−54	*Druffel* [1987]
Okinawa	−42	−13	−29	−23	−33	*Konishi et al.* [1982]
Belize	−60	−12	−48	−42	−27	*Druffel and Suess* [1983]
Florida Keys	−62	−11	−49	−43	−29	*Druffel and Suess* [1983]
Bermuda	−50	−22	−28	−22	−23	*Nozaki et al.* [1978]; *Druffel* [1989]
Average				−40	−39	

All values are per mil.

*The "Suess effect" is the change in $\Delta^{14}C$ between the beginning of the industrial era and 1950 caused by dilution of the ocean's inorganic carbon pool with fossil fuel CO_2 which contains no ^{14}C. Values in parentheses are estimates made on the basis of Suess effects measured elsewhere.

†Pre-1900 surface $\Delta^{14}C$ is either averaged from 1850-1900 coral data or estimated from prebomb coral data from which the Suess effect has been subtracted.

‡Prior to large scale industrialization during the late 19th century atmospheric ^{14}C levels were not exactly 0‰. We adopt a value of −6‰ for atmospheric ^{14}C based on the analysis by *Druffel and Suess* [1983] and subtract this from the pre-1900 coral $\Delta^{14}C$ measurements (estimates) to reconstruct the pre-1900 ocean-atmosphere ^{14}C gradient.

§From P experiment.

Low- and mid-latitude surface values in the C experiment are lower by 10-20‰ than those in the P and B runs, reflecting stronger mixing across the thermocline. Around Antarctica, C values are higher by 20-40‰. Enhanced vertical mixing in the C model thus strongly reduces the equator to pole contrast in surface water ^{14}C in the southern hemisphere.

Meridional Sections Along the GEOSECS Tracks

Figure 10 shows north-south ^{14}C sections through the Pacific Ocean along the western Pacific GEOSECS track for the observations and model runs P, B, and C. Figure 11 shows the same sequence of figures along the western Atlantic GEOSECS track for the observations and model runs. The observations include bomb ^{14}C, while the model results represent the equilibrium prebomb state. Corresponding sections in part 2 (Figures 2 and 3), representing model results for the postbomb era, are plotted on the same scale and can be overlaid on Figures 10 and 11 in order to assess the limits of bomb ^{14}C penetration at the time of GEOSECS. Model results and observations in the Indian Ocean are compared in part 2.

The Pacific observations (Figure 10, top left) show the oldest water in the ocean near 2000 m in the North Pacific with a value of about −240‰ per mil (i.e., 24% depleted relative to the pre-industrial atmosphere). Since ^{14}C decays at a rate of 1% every 83 years, this water has a nominal age of over 2250 years. We have seen, however, that surface water is never equilibrated with the atmosphere and that surface waters around the Antarctic are more than 10% depleted with respect to the atmosphere. Thus newly formed deep water may sink with a nominal "age" of over 1000 years. *Stuiver et al.* [1983] have pointed out that the average age of Pacific deep water is only about 600 years with respect to southern source waters.

Since no deep water formation occurs in the North Pacific, the deep circulation of the Pacific is analogous to that of an estuary. Salty, cold water from the south flows in at deeper

levels while a fresher, warmer outflow develops at 2000-3000 m [see *Gordon*, 1975]. The ^{14}C minimum in the North Pacific is found in the water mass which has traveled the greatest distance, both horizontally and vertically, from the source region. The utility of ^{14}C as a tracer of the slow advection in the deep ocean is vividly demonstrated by the differentiation of water masses according to renewal time in the Pacific GEOSECS sections. Comparable sections of temperature or salinity do not yield such a distinct impression of the form of the ventilation process.

The prognostic P experiment produces a remarkable simulation of the deep Pacific ^{14}C distribution (Figure 10, bottom left). Close inspection shows that its midwater minimum is slightly too old, −250 versus −240‰, and is pressed up against the northern boundary. The big volume of "old" Pacific water, with concentrations less than −180‰ (denoted by light stippling), spreads a little further to the south and does not push up above 1000 m in the North Pacific as the observations indicate. The P experiment's values adjacent to Antarctica (−160‰) are slightly older than the observed values (−140 to −160‰), and the relatively young Antarctic water does not seem to push as far to the north along the bottom as it does in the observations. The P' experiment, with 20% larger gas exchange rates (not shown), produces Antarctic water which closely matches the observed values. The ^{14}C minimum water in the North Pacific is also a bit younger and in closer agreement with the observations.

While it is gratifying that the prognostic model produces a good simulation for the deep Pacific, this result in itself does not tell us very much about the sensitivity of the ^{14}C distribution to the circulation. The B and C results (Figure 10, top and bottom right) from the robust diagnostic model are quite different and yield some appreciation of the sensitivity in the tracer field. Both experiments B and C produce the oldest water in the Pacific adjacent to the bottom in the far North Pacific. Experiment C, with 1 cm^2 s^{-1} vertical diffusion everywhere, produces a ^{14}C minimum of −240‰, whereas experiment B, with the same diffusion formulation
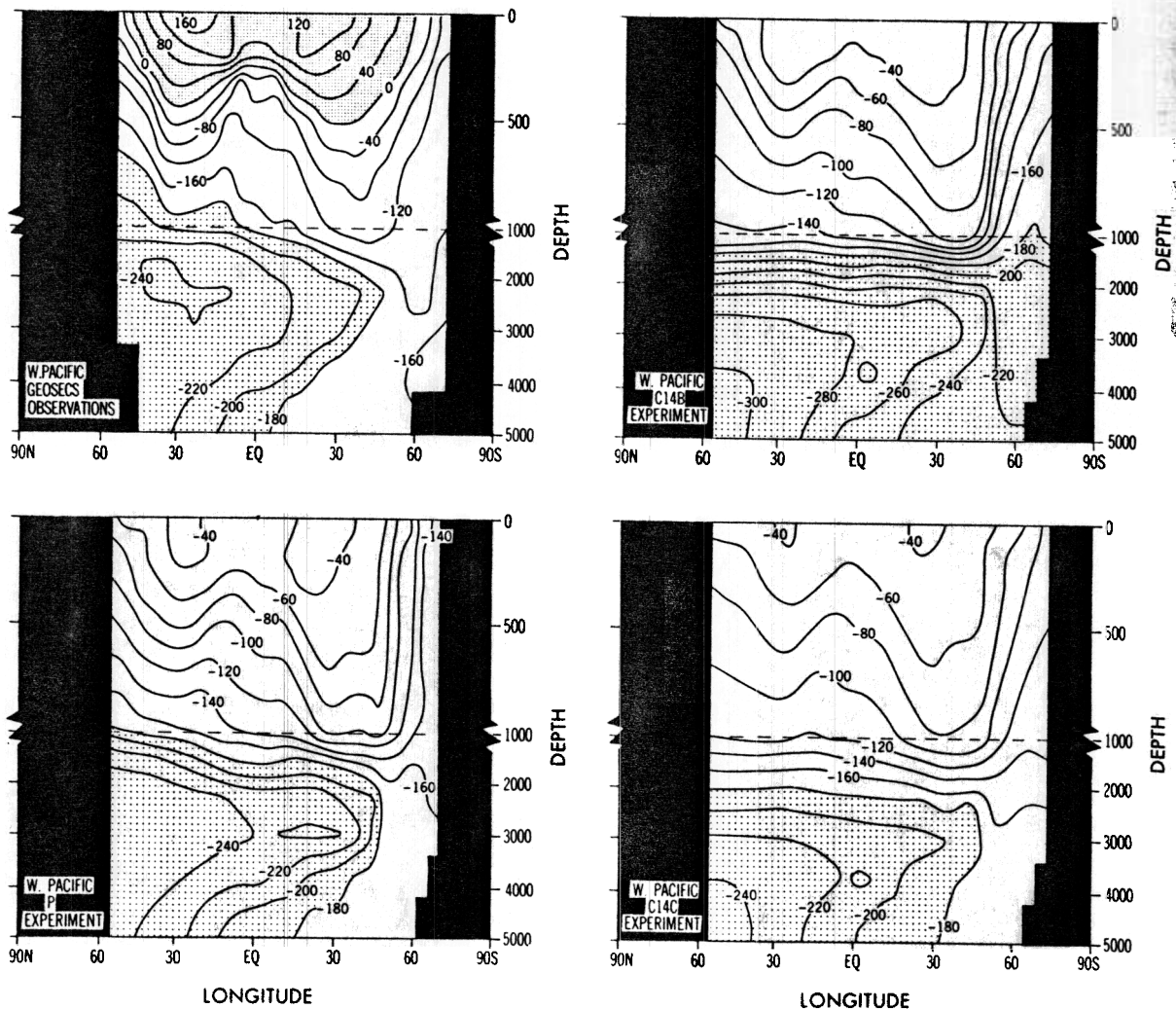
Fig. 10. Latitude versus depth sections of $\Delta^{14}C$ (per mil) along the western Pacific GEOSECS track corresponding to the GEOSECS observations (top left) and experiments P, B, and C. Note that the observations include bomb-produced ^{14}C in the upper ocean. The vertical scale for the upper kilometer is expanded relative to the scale for 1–5 km.

as the prognostic models, produces a minimum of $-300\%c$. The large differences between the B and C model runs dramatically underscores the sensitivity of these model solutions to the transport of ^{14}C through the thermocline via vertical mixing.

The largest contrast between any of the model Pacific sections is found between the B and P experiments, which are identical except for the interior restoring of the temperature and salinity fields in the B experiment. The stippled "old" Pacific water fills the entire deep Pacific in the B experiment all the way down to the Antarctic continent. The isolines of ^{14}C below 1 km in B are almost completely flat, compared with a significant upward slope to the north in both the prognostic model and observations. These differences suggest that the restoring of temperature and salinity to the observed values has somehow suppressed the processes ventilating the deep Pacific basin, while the anomalous temperature and salinity fields of the prognostic model have produced a much more realistic circulation.

The major difference between the Atlantic and Pacific ^{14}C distributions is the impact of the high-latitude source waters. The bottom water which forms in the North Atlantic origi-

nates from warm, salty water in the upper thermocline [Warren, 1981]. When this water flows poleward and outcrops, the atmosphere extracts tremendous quantities of heat, lowering its temperature as much as 10°C. This water mass conversion produces a dense, salty water mass in the Norwegian and Greenland seas which is an important component of North Atlantic Deep Water. The ^{14}C content of newly formed North Atlantic Deep Water is thus quite high because of the exposure of its source waters to the atmosphere. In the GEOSECS observations (Figure 11, top left) we see newly formed NADW tagged to some degree with bomb ^{14}C. Local surface waters around the Antarctic, in contrast, are quite fresh. The greater part of bottom waters which form around Antarctica must originate from saltier, low ^{14}C water upwelled from depth. The exposure of this water to the atmosphere is relatively brief compared with the isotopic equilibration time, and its ^{14}C content stays quite low.

The observed abyssal water in the Atlantic (Figure 11, top left) contains water from both these sources. The $-100\%c$ NADW fills up the North Atlantic below 1 km, while the $-160\%c$ bottom water from the Antarctic intrudes into the
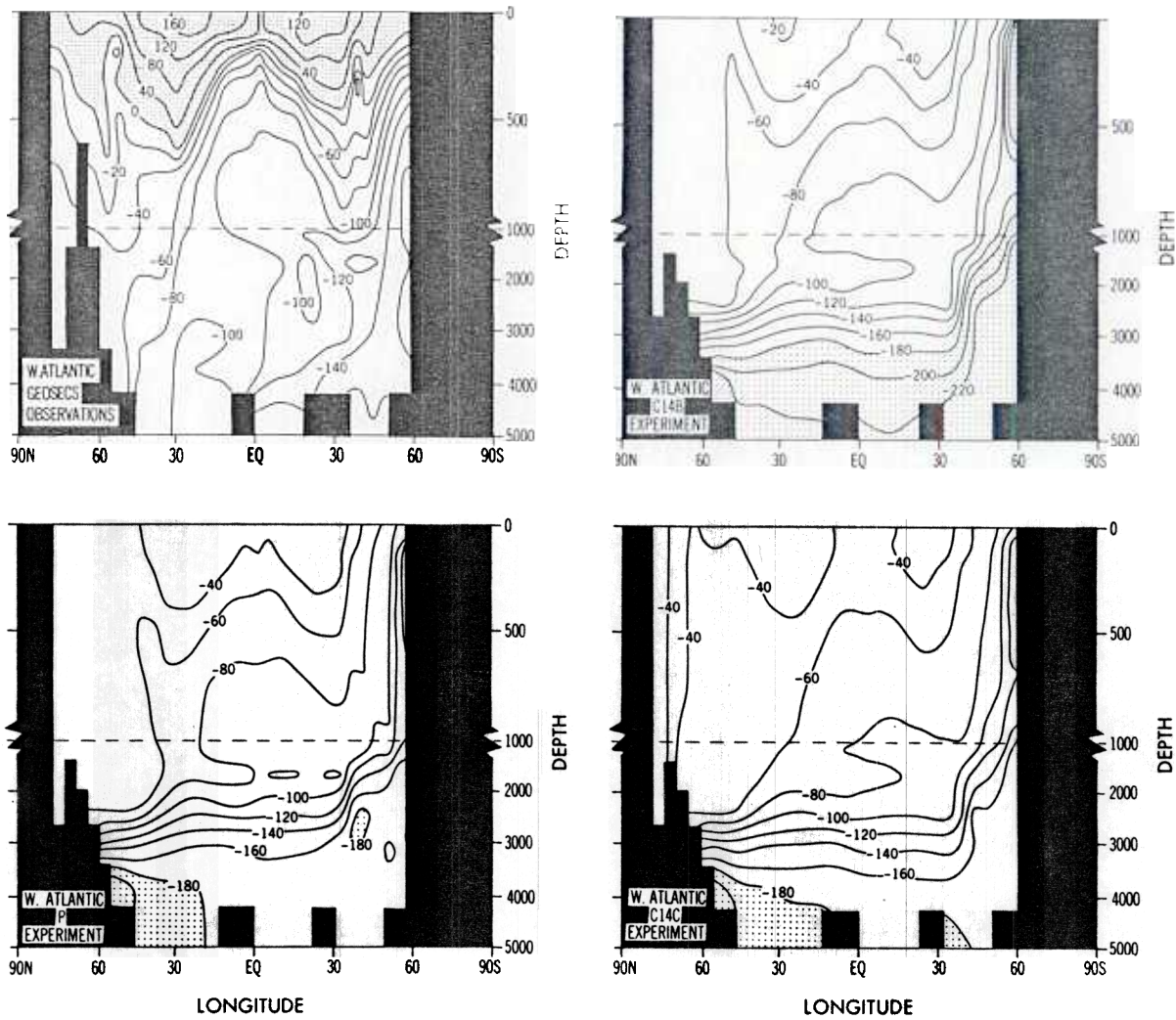
Fig. 11.   Latitude versus depth sections of $\Delta^{14}C$ (per mil) along the western Atlantic GEOSECS track corresponding to the GEOSECS observations (top left) and experiments P, B, and C. The vertical scale for the upper kilometer has been expanded.

South Atlantic along the bottom. One also sees a tongue of $-100\%_0$ Antarctic Intermediate Water near 1 km beneath the equatorial and south temperate regions. The prognostic model simulation (Figure 11 bottom left) produces a North Atlantic Deep Water with a ^{14}C content of about $-80\%_0$, but the model's NADW pushes southward between 1000 and 2000 m rather than filling the North Atlantic basin. The model's North Atlantic bottom water is very weakly ventilated by flow from the south and by vertical mixing with overlying water.

The Atlantic simulations in the B and C experiments (Figure 11, top and bottom right) are qualitatively similar to the prognostic model. The deep water in the B case is $20\%_0$ older than in the prognostic case primarily because the Antarctic end member is older, as illustrated in the Pacific sections. Higher rates of vertical mixing make bottom water younger in the C case but also nearly obliterate the ^{14}C signature of Antarctic Intermediate Water.

Distribution of ^{14}C Along a Density Surface

Figure 12 shows results for the robust diagnostic experiments B and C and the observations along the $\sigma_\theta = 27.75\%_0$ density surface. This surface corresponds to a potential density, referred to surface pressure, of 1027.75 kg m^{-3}. This surface is found near 1500 m in the Atlantic and deepens to 2500 m going around to the North Pacific. The 27.75 surface falls in the middle of the ^{14}C minimum in the North Pacific.

The 27.75 surface outcrops in high latitudes of the North Atlantic where it has picked up a trace of bomb ^{14}C. Values decrease steadily southward in the Atlantic toward the Antarctic, where fairly constant values are found around the globe. *Broecker* [1979] has pointed out that the north-south gradient in ^{14}C in the Atlantic Ocean is mainly a result of mixing between the northern and southern source waters, such that the radioactive decay signal is quite small and hard to detect.

The 27.75 surface corresponds closely to the isopycnal surface examined by *Reid* [1981] in his review of the mid-depth circulation of the ocean. Reid demonstrated that the circulation in this depth range is organized into zonal flows which are connected by tongues of northward and southward flowing water along the boundaries and along deep topographic features, much like the wind-driven circulation in the upper ocean. Isolines of ^{14}C in the observations appear to have a purely zonal orientation. If the flow at these depths
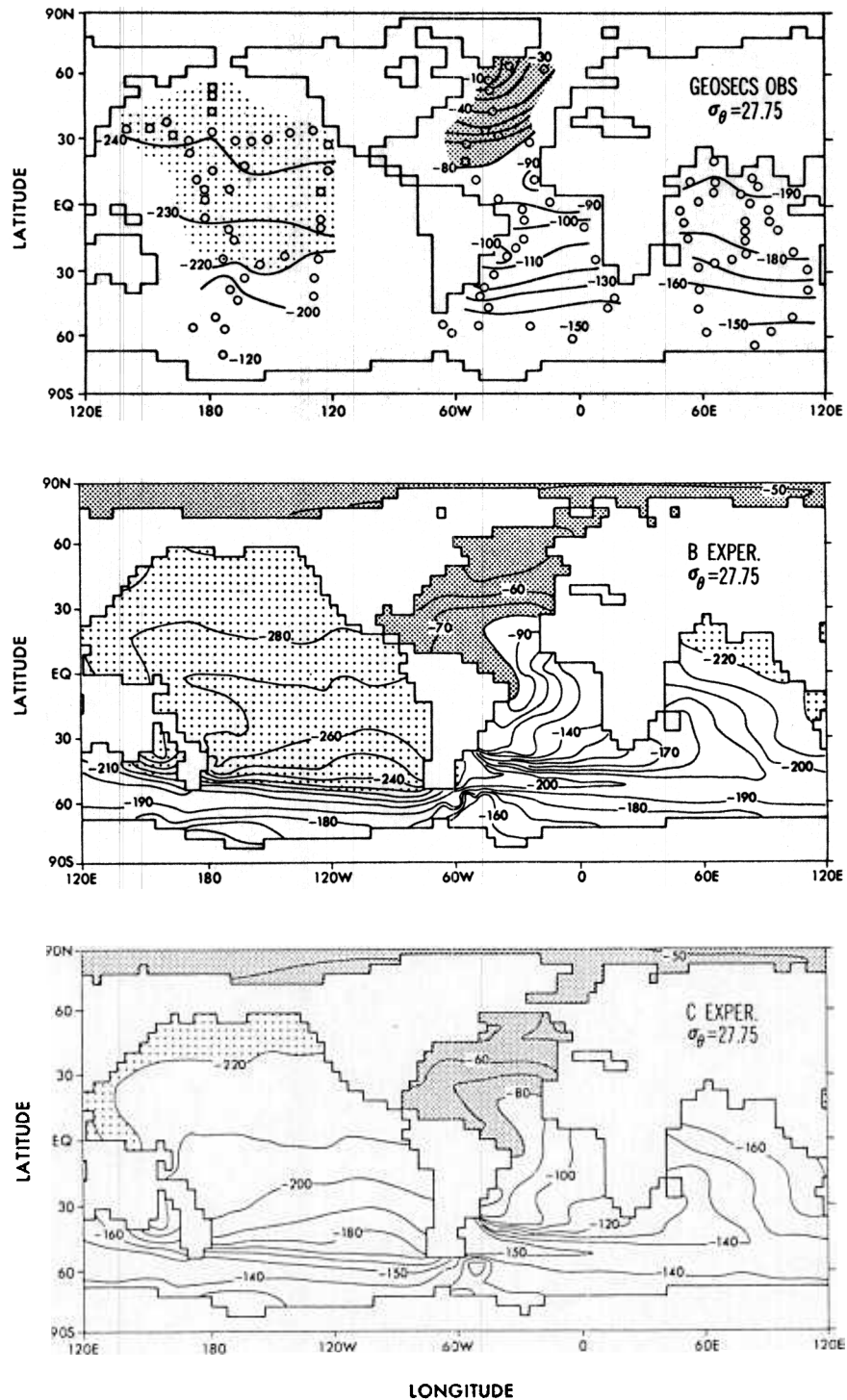
Fig. 12. $\Delta^{14}C$ on the potential density surface σ_θ = 27.75 corresponding to the (top) GEOSECS observations, (middle) experiment B, and (bottom) experiment C. We have not attempted to contour the observations in most areas of the southern ocean. Oceanographic structures are apparent in the data but cannot be resolved with the GEOSECS sampling gird.

is organized as Reid described, why are these patterns not evident in the observed ^{14}C distributions? The model results show the ^{14}C isolines being distorted by a flow pattern similar to that described by Reid. The model, being quite diffuse, spreads its north-south trending tongues over wide areas. If these features are present in ^{14}C distributions, the coarseness of the GEOSECS sampling grid and its limited coverage along the continental margins do not allow these

features to be contoured. The GEOSECS tracks apparently miss very important signatures of the deep circulation.

Meridional ^{14}C Transport

In the prebomb state the ocean's ^{14}C distribution is not changing. Within a column of water, a balance must exist between the surface source of ^{14}C from the atmosphere, redistribution by transport, and radioactive decay. In Figure
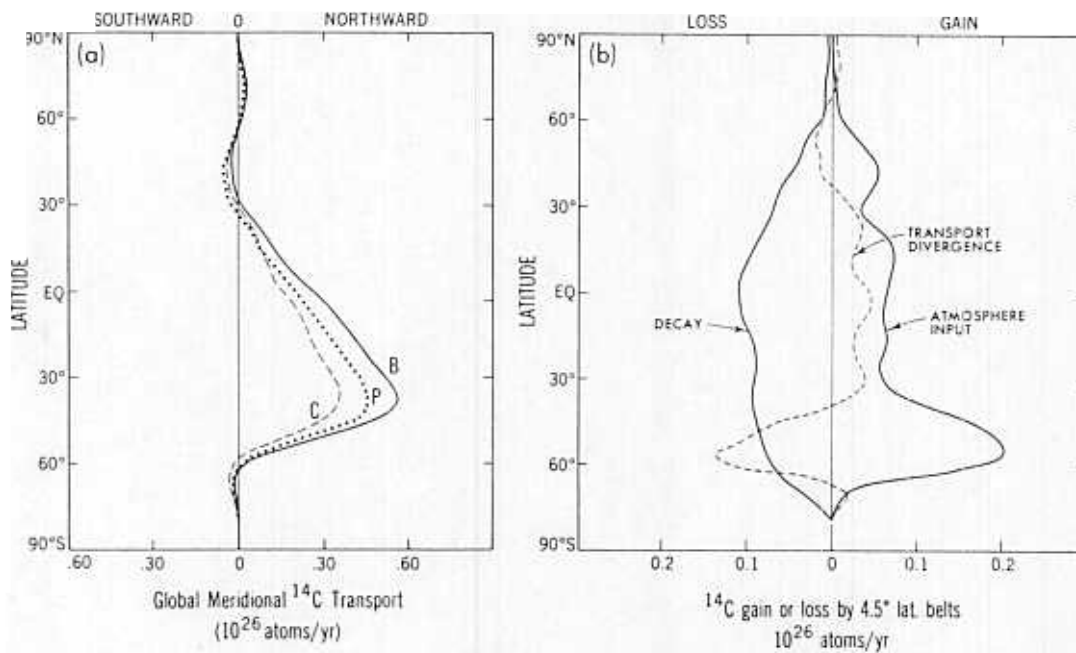
Fig. 13. (a) Latitudinal distribution of the northward ^{14}C transport in the model by advection and mixing, zonally and vertically integrated, for experiments P, B, and C (units are 10^{26} atoms yr^{-1}). (b) Gain or loss of ^{14}C within 4.5° model latitude belts, zonally and vertically integrated, for the P experiment (units are 10^{26} atoms yr^{-1}). Carbon 14 budgets for individual latitude belts are separated into three terms: loss to decay within the ocean volume defined by the latitude belt, input from the atmosphere, and the transport divergence, which is the difference between the northward ^{14}C transport (from Figure 13a) across the northern and southern bounds of each belt.

13 we show how the ^{14}C balance is maintained in the various experiments by plotting the zonally and vertically integrated transports, losses to decay, and atmospheric inputs by latitude belts. Figure 13a shows how the northward transport of ^{14}C by advection and diffusion is distributed in the P, B, and C experiments. The northward transport in each case is at a maximum near 40°S and gradually declines toward the north. Transports in the C experiment are a little more than half those of the B experiment, while the P transports fall in between.

The significance of the transports can be more easily appreciated by looking at the transport divergence. The transport divergence is simply the difference in northward transport between adjacent latitude belts. This quantity can be directly compared with the gain of ^{14}C by the latitude belt from atmospheric input and the loss of ^{14}C by decay. The transport divergence, loss by decay, and atmospheric input for the P experiment are shown in Figure 13b. The plot of ^{14}C decay has a broad maximum through the low and middle latitudes of the ocean which simply reflects the greater area of ocean in these latitude belts. Throughout low and middle latitudes, losses to decay are balanced by atmospheric input and a net convergence of ^{14}C by transport. In higher latitudes the net transport is divergent, and inputs of ^{14}C from the atmosphere must balance both decay and net transport losses.

Atmospheric sources of ^{14}C are much larger in the southern hemisphere than in the northern hemisphere. This finding is not surprising, given the observation that the ^{14}C content of high-latitude surface water is much more deficient relative to the atmosphere in the southern hemisphere than in the northern hemisphere. Note from the latitude distribution that the peak atmospheric input is found in the circumpolar region, where surface waters are modestly de-

pleted in ^{14}C but gas exchange rates are highest. Our sea-ice inhibition of gas exchange makes atmospheric ^{14}C inputs in the higher southern latitudes much less significant. The North Atlantic does not appear to add much ^{14}C to the rest of the ocean when results are plotted this way. This is because its northward flowing source waters have nearly the same ^{14}C content as the southward flowing deep water. The North Atlantic does, however, send high ^{14}C water southward at a deeper level, and in this sense it should be considered an effective source of deep sea ventilation.

One can appreciate the role of vertical mixing in the ^{14}C budgets by comparing the relative contributions of transport divergence and atmospheric input. Between 35°N and 35°S, atmospheric input balances about two thirds of the decay, and the transport balances only one third. This means, in effect, that vertical mixing (by both vertical diffusion and advective stirring) is transporting about two thirds of the new ^{14}C needed to balance decay down the water column.

Differences in the relative roles of vertical mixing and horizontal transport account for the differences in ^{14}C transport between the B and C models in Figure 13a. Experiment C, with the higher (1 cm^2 s^{-1}) vertical diffusion coefficient in the upper kilometer, has the smallest northward transport because more of the ^{14}C needed to balance decay in its low- and mid-latitude regions comes in locally from the atmosphere. A useful diagnostic of the roles of vertical mixing and northward transport can be seen in the comparison of surface water ^{14}C distributions in Figure 9. Experiment C generally has the lowest surface ^{14}C concentrations (i.e., the biggest ocean-atmosphere gradient). The C experiment's lower surface values reflect the importance of its more efficient downward transport of ^{14}C via vertical mixing. The greater northward transports across 40°S in the B experi-

ment are supplied by enhanced high-latitude inputs associated with very low southern ocean surface values.

In this context, one might be curious why the P experiment should have such a significantly smaller northward transport than B when their vertical diffusion formulations are the same. A comparison of the surface water ^{14}C distributions between the two models in Figure 9 shows that the P experiment's surface values are 10‰ lower throughout the tropical Pacific and Indian oceans. Differences between the prognostic and robust diagnostic overturning diagrams in Figure 4 explain why. The deeper penetration of the prognostic model's wind-driven equatorial and subtropical overturning cell in the southern hemisphere is primarily a feature of the southern Pacific and Indian oceans. Wind pumping enhances the total vertical mixing in the prognostic model and increases the atmospheric input in low and middle latitudes.

The importance of vertical mixing in the ocean's ^{14}C balance may seem surprising to some readers, and one might be tempted to argue that there is too much vertical mixing even in the B and P cases. If the vertical diffusion coefficients in B and P were significantly smaller, such that meridional transport was relatively more important, predicted ^{14}C values in the surface layer would be closer to atmospheric equilibrium. This consequence would force model predictions to be at variance with the observational constraints. As we showed in Table 5, surface values in the P experiment are in reasonably good agreement with pre-1900 observations.

Another way of looking at the relative roles of meridional transport and vertical mixing is to consider that ^{14}C transport would be much more important if the gas exchange equilibration time for ^{14}C were shorter and more like equilibration times for other gases. Transport of ^{14}C is less important than vertical mixing in the model's ^{14}C balance because bottom water of Antarctic origin does not pick up much new ^{14}C from the atmosphere during its brief contact with the atmosphere. Recall that the vertical gradient of ^{14}C in the ocean is caused as much by the low ^{14}C concentrations in Antarctic surface water as it is caused by decay.

Figure 14 shows how the northward transport of ^{14}C in the P experiment breaks down vertically at 35°S. The net northward transport, indicated by the dotted line at 0.5×10^{26} atoms yr^{-1} arises largely from the difference between larger northward transports in the bottom and intermediate-depth layers and smaller southward transports in mid-depth water. The large southward Ekman transport in the surface layer is totally compensated by northward flow in the layers between the surface and 600 m.

At latitudes further south the transport of ^{14}C at the surface is strongly northward, as the water flowing equatorward under the roaring 40s is actively picking up ^{14}C from the atmosphere. Between 45°S and 35°S the northward transport of ^{14}C at the surface diminishes and is replaced by the strong northward transport at intermediate depths seen in Figure 14. In pointing this out, we are alerting the reader to a major finding of part 2. The water masses transporting ^{14}C northward in layer 6 (755 m) at 35°S become loaded with bomb ^{14}C in our model simulations. These water masses form near 45°S, approximately the latitude where Subantarctic Mode Water forms in the real ocean [McCartney, 1977].
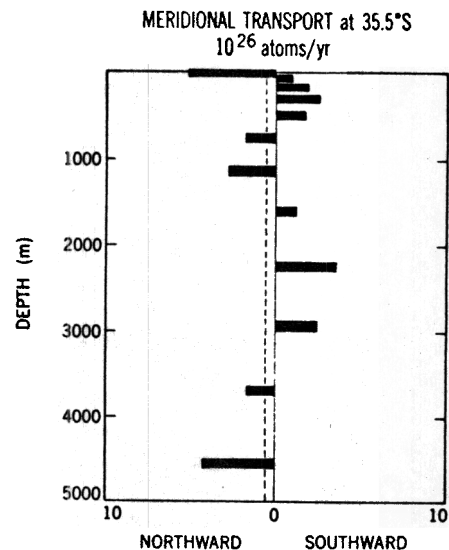
MERIDIONAL TRANSPORT at 35.5°S
10^{26} atoms/yr

Fig. 14. Vertical distribution of the meridional ^{14}C transport by advection and mixing, zonally integrated, at 35.5°S in the P experiment (units are 10^{26} atoms yr^{-1}). The dotted line represents the average northward transport at this latitude plotted in Figure 13a.

DISCUSSION

Differences Between Prognostic and Robust Diagnostic Models

At the outset of this project, we were concerned that our basic prognostic model would produce a poor ^{14}C simulation because its predicted temperatures and salinities in the interior chronically deviate from observed values. Hence the robust diagnostic model was constructed in addition to the prognostic model. We anticipated a better simulation from a model whose density field was at least consistent with the observed distribution of density in the ocean. A fairly long restoring time constant, 1/(50 years), was chosen to minimize the artificial sources of heat and salt produced by the restoring terms. However, it is very clear from the ^{14}C distributions that the model with the unrealistic hydrography produces the most realistic deep circulation, while the model with the realistic hydrography (and artificial heat and salt sources and sinks) produces a rather poor deep circulation.

The features which reveal the most significant differences between the B and P experiments are (1) the Pacific ^{14}C minimum lying on the bottom in B and at mid-depths in the prognostic model, (2) the lack of any upward slope in the B experiment's Pacific ^{14}C isolines viewed in meridional section, (3) the B experiment's very old ^{14}C values adjacent to Antarctica, and (4) the enhanced transports of NADW and Pacific AABW in the prognostic model. Points 1, 2, and 3 are illustrated in Figure 10, and point 4 is illustrated in the overturning diagrams in Figure 4. We find in each of these cases that the alteration of the density structure by the restoring terms suppresses advection or convection in important areas.

Figure 15 shows maps of vertical velocity in the prognostic and RDIAG1 flow fields at the base of layer 7 (1347 m). In the North Pacific the prognostic model shows widespread upward motion, whereas RDIAG1 has both downward and upward motion. The tendency for ^{14}C isolines to shoal toward the north in the prognostic model (see Figure 10) but to stay flat in the diagnostic model seems easily explained in
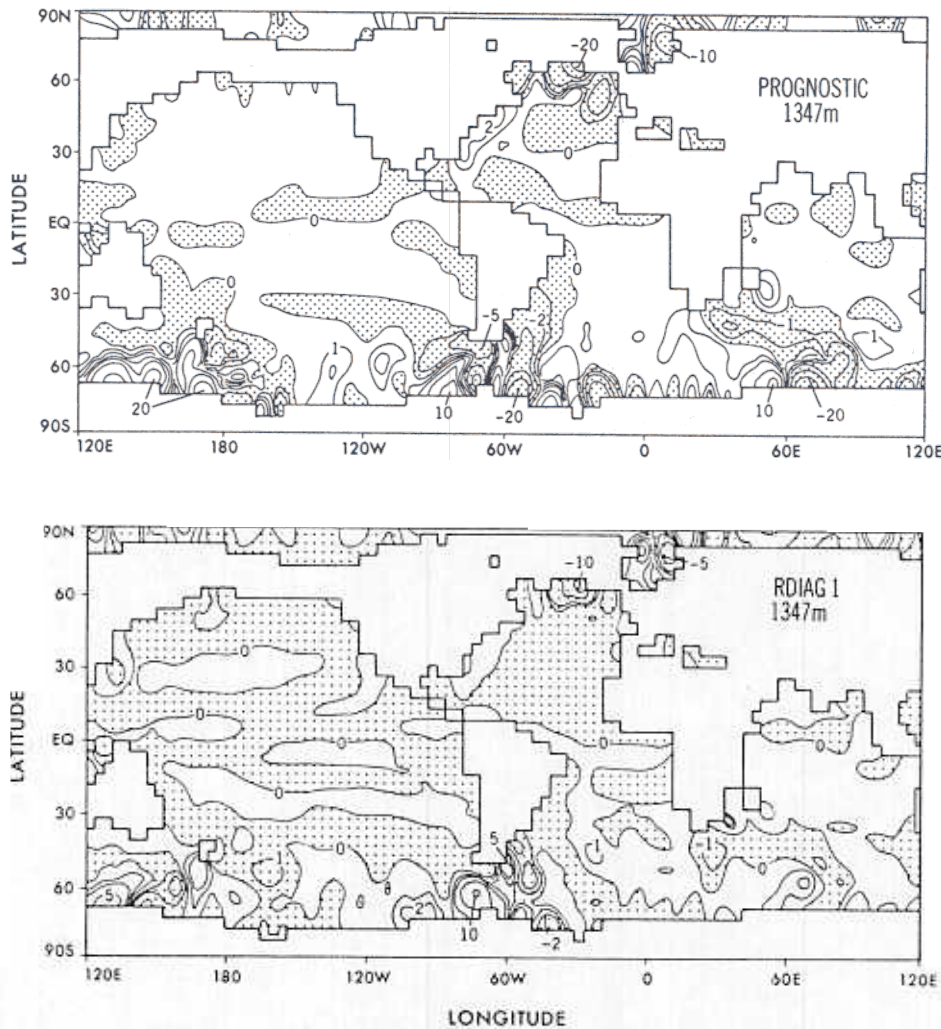
Fig. 15. Comparison between vertical velocities (units are 10^{-4} cm s^{-1}) at 1347 m in the (top) prognostic and (bottom) robust diagnostic models. Stippling and contour conventions are the same as in Figure 6.

terms of differences in vertical motion. A comparison of model temperatures at layers 7 and 8 with observed temperatures (not shown) shows that prognostic model temperatures are much warmer (as much as 6° warmer) in the North Pacific. Given the tendency toward much warmer equilibrium temperatures in this area, it is evident that the temperature restoring term in the diagnostic model is removing significant amounts of heat, thereby increasing density in situ. Consequently, the widespread upwelling observed in the prognostic solution is suppressed.

Figure 15 shows that organized vertical motions near Antarctica at 1350 m are much more intense in the prognostic model than in the RDIAG1 model. Figure 16 compares the frequency of convection at the base of layer 4 (371 m) between the prognostic and RDIAG1 models. Convective overturning in the southern ocean is much more extensive in the prognostic model. From Figures 15 and 16 it is easy to see why ^{14}C concentrations adjacent to Antarctica are so much younger in the P experiment relative to B. Most of the overall differences in apparent ^{14}C "age" of the deep water in these two experiments can be traced to the initial values set in the Antarctic.

We attribute these prognostic versus diagnostic differences in convection frequency and vertical advection to the restoring terms in the diagnostic model here, as well. When the hydrographic properties of the surface water are forced with annually averaged temperatures and salinities but deep-water values are restored toward observed temperatures and salinities, the robust diagnostic model creates denser water at depth than can be brought down from the surface. This produces a slightly more stratified water column which suppresses vertical motions and the frequency of convection. The deep water of the prognostic simulation is not as dense, but its properties can at least be traced back to the particular annually averaged boundary conditions used to force the model.

Analysis of the abyssal overturning in the deep Pacific shows that the deep circulation is about 40% stronger in the prognostic model. This difference, together with the larger upward velocities below the thermocline in the North Pacific discussed above, accounts for the shift in the ^{14}C minimum away from the bottom in the prognostic model.

Warren [1970] summarizes evidence for deep western boundary currents in the South Pacific. He finds evidence for a strong density gradient normal to the Tonga-Kermadec Ridge between 2 and 4 km depth. This gradient is consistent with a vigorous northward flow near the bottom with weak flow at the base of the thermocline. The oldest and most saline waters are
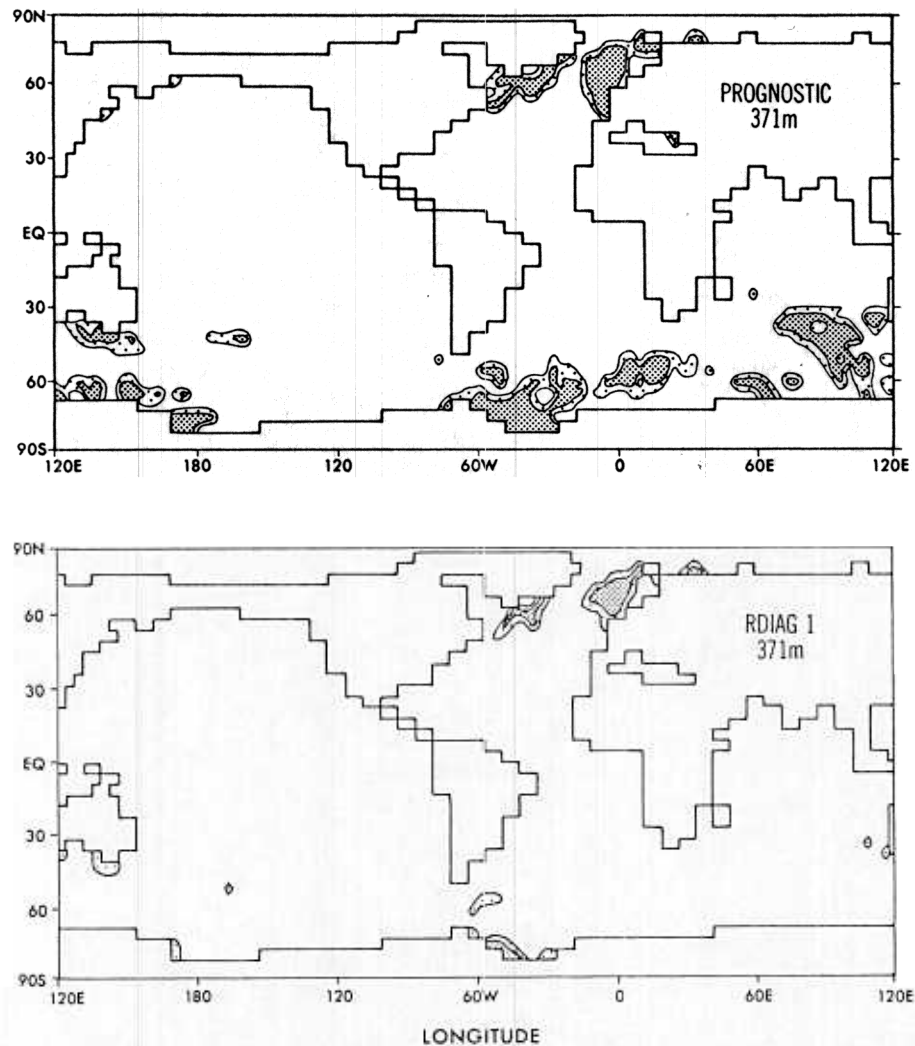
Fig. 16.   Comparison between convection frequency at 371 m in the (top) prognostic and (bottom) robust diagnostic models. Stippling and unit conventions are the same as in Figure 6.

adjacent to the ridge, and most of the temperature and salinity gradients are confined to within a few hundred kilometers of the ridge. When these observations are compared with the prognostic model, we find a similar east-west density contrast in the model at 20°S. A decrease in temperature of 0.35°C from east to west exists in the four grid boxes adjacent to the deep western boundary of the model. Contrary to observations, the salinity gradient in the model compensates rather than supports the temperature gradient.

Several interesting features of the prognostic and diagnostic models are illustrated here. First, the prognostic model appears to spread the density gradient driving the deep flow over a much greater distance in order to maintain a balance with its large mixing terms. Second, we find that the orientation of the salinity field in the deep Pacific is almost flat in the prognostic model, in contrast with the observed field, with slightly higher salinities in the North Pacific than in the south. (This is caused, in part, by the lack of a significant intermediate-depth salinity minimum in the North Pacific.) The prognostic model builds a bigger east-west temperature contrast than is observed in order to compensate for the weak reversal in the salinity field. Third, the relatively steep temperature and salinity gradients in the real world, which drive the deep geostrophic flow, are not resolved in the data

field used by the restoring terms of the diagnostic model. A much smaller density gradient is thereby imposed on the diagnostic model, and it acts to suppress the diagnostic model's deep Pacific flow. A similar situation exists in the North Atlantic. The prognostic model develops a strong deep flow in a different depth range than that occupied by the deep flow in the real ocean. The prognostic model builds a pressure head to accommodate this flow, while the restoring terms in the robust diagnostic models try to suppress it.

To summarize, the restoring terms in the robust diagnostic model act to suppress advection and convection in several critical areas. We have not found any instances where the restoring terms improve the model's ^{14}C distribution. Surprisingly, the ^{14}C simulations suggest that the erroneous temperature and salinity fields produced by the prognostic model do not degrade the circulation. In some cases, we find that the prognostic model's local alteration of the observed temperature and salinity structure actively accommodates deepwater flows of the correct magnitude.

Northern Versus Southern Sources of Deep Water

Without question, the worst feature of the model's ^{14}C simulation is its failure to correctly simulate the large and
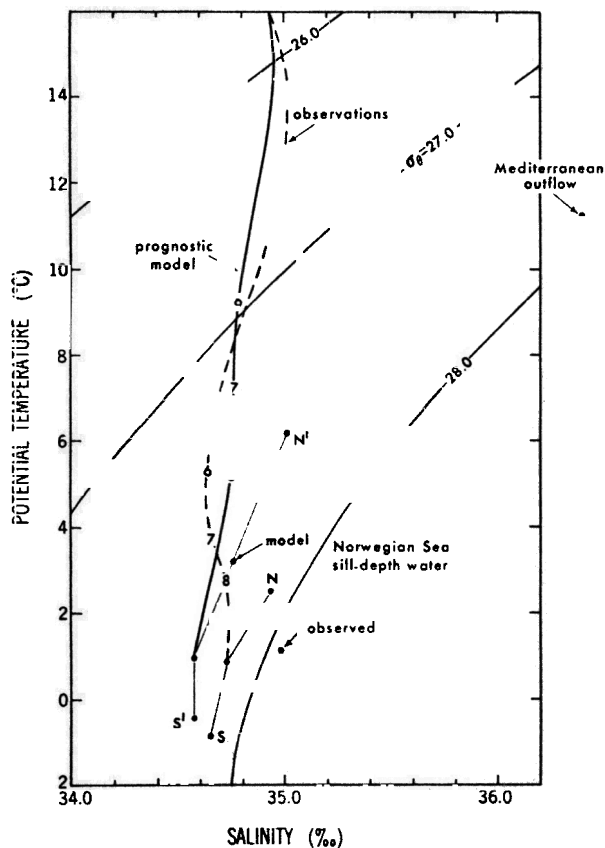
Fig. 17. Potential temperature versus salinity plot showing the global average *T-S* compositions corresponding to the 10 lower layers of the prognostic model (solid line) and the global average observations at model layer depths (dashed line). Contours of potential density equal to 26.0, 27.0, and 28.0‰ are drawn for reference. Points labeled N and S represent *T-S* compositions of northern and southern sources of deep water according to Broecker *et al.* [1985b]. The points labeled N' and S' represent the model's North Atlantic Deep Water and the model's most dense bottom water adjacent to Antarctica, respectively. The *T-S* composition of Mediterranean outflow water is taken from Transient Tracers in the Ocean (TTO) station 113, 1238 m. The *T-S* composition of Norwegian Sea sill-depth water is taken from GEOSECS station 19, 632 m.

relatively young NADW water mass in the North Atlantic. This is easy to understand from the hydrographic point of view, because the model does not form a water mass dense enough to fill the North Atlantic basin. As a result, the only genuine bottom water in the model is formed adjacent to Antarctica. The densest bottom water is found adjacent to Antarctica in the Pacific sector of the southern ocean. Bottom water with a slightly lower density forms in the Atlantic sector.

Figure 17 shows a temperature-salinity diagram for the observed and prognostic model global averages at each depth level. The *T-S* composition for the North Atlantic and Antarctic bottom waters formed in the real ocean are labeled as N and S. The densest bottom water in the model is labeled as S'. The composition of the model's NADW south of Greenland is labeled as N'. For comparison the *T-S* compositions of Norwegian Sea sill-depth water in the model and as observed are shown, along with the composition of the Mediterranean outflow. The mean compositions of real ocean water at subthermocline model depths 6, 7, and 8 are labeled, along with the model means. Layer 6 (754 m) in the

real ocean corresponds to the depth of the salinity minimum, while layer 8 (1622 m) corresponds to the top of the North Atlantic Deep Water. Model *T-S* properties at these depths plot as much as 4° warmer than the observed properties, and there is no salinity minimum in the model's global mean.

There is no Mediterranean outflow in the model. The injection of salty Mediterranean water into the North Atlantic thermocline allows very dense bottom water to form in the Norwegian Sea when thermocline density surfaces outcrop and give up heat to the atmosphere. Reid [1979] has shown that salt from the Mediterranean and silica from intermediate waters farther south reach the areas where Norwegian Sea deep waters form. He maintains that the Mediterranean salinity is a critical factor in the formation of the NADW. Reid's argument is easily visualized in the *T-S* plot in Figure 17. Given its high salinity, any remnant of the Mediterranean outflow reaching the surface in the Norwegian Sea can be cooled to produce a water type more dense than any other water in the ocean. As this dense Norwegian Sea water flows over the sills and entrains North Atlantic water it remains dense enough to sink to the bottom of the North Atlantic basin. The model's Norwegian sea sill-depth water, on the other hand, is not distinguishable from bottom water in the rest of the ocean in terms of density. As it attempts to flow out of the Norwegian Sea it mixes with North Atlantic water and produces a water mass which is distinctly less dense at deep-sea pressures than bottom water from Antarctica.

The Circumpolar Overturning Cell

The existence of strong, wind-driven vertical water movements in the southern ocean were originally deduced by Deacon [1937] based on water mass properties. Deacon interpreted the temperature and salinity structure in terms of an upwelling poleward of the circumpolar current feeding into an equatorward Ekman transport. According to Deacon, downwelling on the north side of the circumpolar current spreads to the north as Antarctic Intermediate Water, while deep water from the major ocean basins to the north spreads to the south to feed the upwelling south of the current. A diagram of this overturning circulation appears in Sverdrup *et al.*'s [1942] *The Oceans* and has been reproduced in many other textbooks. One implication of this two-dimensional diagram is that the overturning circulation in the upper part of the southern ocean is zonally symmetric.

This classical view was questioned by Gill and Bryan [1971] on the basis of theory and numerical experiments and by McCartney [1977] on independent empirical evidence. Gill and Bryan carried out numerical experiments in an idealized southern hemisphere ocean basin, studying a simulation of the ocean circulation with and without a Drake Passage. Without a Drake Passage the thermohaline circulation penetrates to the polar wall, with the region of most intense sinking located at the extreme southern boundary. When the equivalent of a Drake Passage is included, the region of maximum sinking moves equatorward to a position along the eastern boundary just north of the point where the circumpolar current enters the Drake Passage. From these experiments Gill and Bryan concluded that Antarctic Intermediate Water was formed largely by intense downwelling just upstream of the Drake Passage off the coast of Chile. A similar idea was worked out independently by McCartney [1977], who found that deep winter mixed layers along the
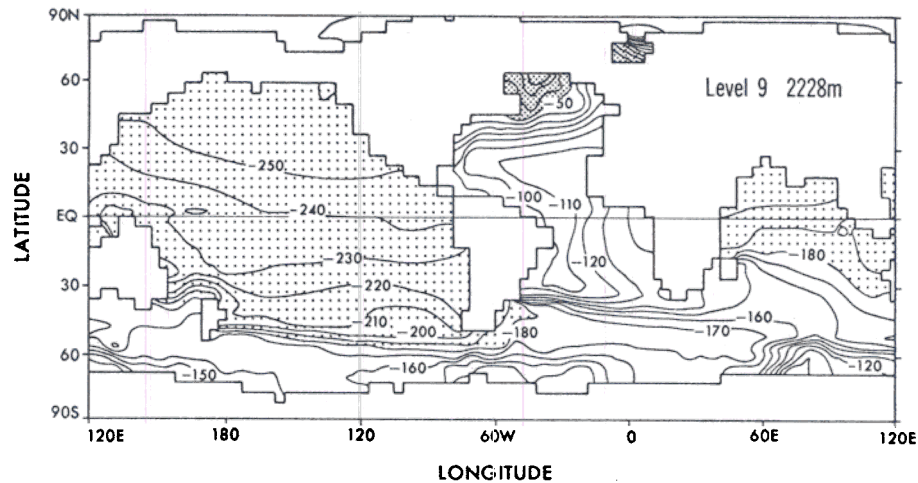
Fig. 18. Distribution of $\Delta^{14}C$ predicted by the prognostic model at level 9 (2228 m) for the year 1972 illustrating the series of radiocarbon fronts in the circumpolar region. Level 9 corresponds to the depth of the ^{14}C minimum in the North Pacific and the lowest level of NADW in the model. Bomb ^{14}C has penetrated the most northern part of the North Atlantic in the stippled area.

northern side of the circumpolar current formed thick low-stability layers below the seasonal thermocline, which he named the Subantarctic Mode waters. The mode waters become cooler, fresher, and denser along the path of the circumpolar current between the western Indian Ocean and the eastern South Pacific. McCartney has shown that the mode waters forming just upstream from the Drake Passage have been cooled and freshened enough to match the properties of the low-salinity intermediate water in the South Pacific.

The geometry of the present numerical model is far more complex than that of Gill and Bryan [1971], and the vertical velocity pattern shown in the top panel of Figure 15 is correspondingly more complex. Sinking on the equatorward side of the Antarctic Circumpolar Current is concentrated at a few longitudes. The top panel of Figure 15 shows prominent areas of sinking water near the tips of New Zealand, South America, and Africa. Downward motions along the circumpolar current extend to great depth and involve more than just intermediate waters.

Figure 18 shows the predicted distribution of ^{14}C at 2228 m (level 9). The ^{14}C distribution shows two sharp ^{14}C fronts within the circumpolar region, one in the South Atlantic and one in the South Pacific which are produced in response to the pattern of vertical motion in the top panel of Figure 15. The Pacific front separates the very "old" waters of the North Pacific from the intermediate aged waters near Antarctica. The Atlantic front separates the "young" water with a source in the North Atlantic from Antarctic deep water. The existence of these fronts in the model shows that the circumpolar waters are a relatively well mixed reservoir separating a distinct North Atlantic source region and a North Pacific sink region.

Unfortunately, the spacing of the GEOSECS radiocarbon stations was not planned to resolve the sharp gradients in ^{14}C that are predicted by the model. The ^{14}C front in the South Pacific forms a very prominent feature in the west Pacific GEOSECS radiocarbon section (top panel of Figure 9), even though the nearest radiocarbon stations are about 700 km apart in this area. The more closely spaced GEOSECS hydrographic stations show a very strong front in silica at

47°S. In the silica section (not shown), isolines of low silica, characteristic of the upper ocean, bend down sharply between 2000 and 3000 m in front of the southern limit of high-silica Pacific deep water, in accord with the model's prediction of deep downwelling off the southern tip of New Zealand.

In connection with their numerical experiments, Gill and Bryan [1971] pointed out that in the Drake Passage zonally averaged east-west pressure gradients can exist only in the zone below the sill connecting South America with Antarctica. Thus all net meridional flow above the sill has to be balanced by purely inertial or frictional effects. Geostrophically balanced, zonally averaged north-south flows cannot exist in the zone of the Drake Passage above the sill. This accounts for the deep penetration of the overturning cell shown in Figure 4 and the downward motions giving rise to the ^{14}C fronts in the top panel of Figure 15.

In the model, some friction is apparent, as half the northward Ekman flow at the surface (~ 25 Sv) is balanced by southward flow above 1000 m. Between 1000 m and the depth of the sill, southward flow across the latitudes of the Drake Passage is very weak. With respect to advection, the sill connecting South America to Antarctica in the model is effectively the base of layer 9 at 2559 m. About 13 Sv of southward flow occur below in layers 10 and 11. A detail of the radiocarbon distribution at level 11 in Figure 19 shows two tongues of water moving toward the southwest in the South Pacific and Indian oceans between 55° and 60°S.

With the exception of surface waters and some southward flow in the upper 1000 m, it is only in these deeper layers where direct water transport occurs across the circumpolar belt. Figure 19 shows that the radiocarbon concentration in these tongues is about -170 to $-180\%_c$, hardly prime examples of Pacific or Indian ocean deep water. In its temperature and radiocarbon content, the southward flowing water is almost indistinguishable from bottom water flowing north in layer 12. Much of the Antarctic Bottom Water simply recirculates within the deeper layers of the model at fairly high latitudes, leaving only a fraction of the original AABW to penetrate further north. Much of the bottom water flow north of 45°S seen in the overturning diagram in the top panel
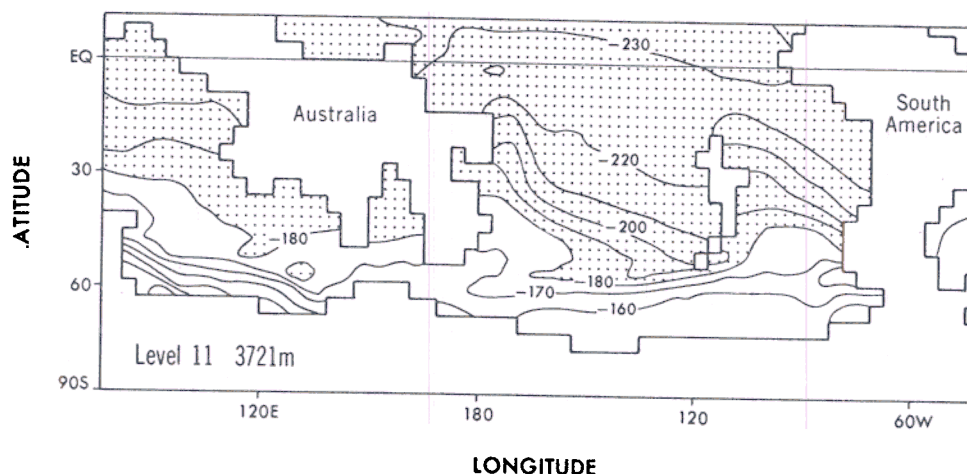
Fig. 19. Detail from the southern Pacific and Indian oceans of the distribution of $\Delta^{14}C$ predicted by the prognostic model at level 11 (3721 m). The southwestward trending tongues southeast of New Zealand and south of Australia represent the only significant southward flows across the circumpolar region in the deep water.

of Figure 4 carries recycled deep water. In contrast to the Deacon view, the water which upwells at 60°S around Antarctica in the model is largely circumpolar water containing relatively little deep water from the major ocean basins to the north.

The meridional circulation in the circumpolar region thus takes on a completely different look in the model compared with the classical view of Deacon and Sverdrup. Relatively small volumes of water flow across the circumpolar region below 1000 m to ventilate the deep Pacific and Indian ocean basins. The circumpolar deep water appears to be directly ventilated itself, while the deep basins to the north are only weakly ventilated by advection.

Comparison With Other Simulations

The *Stommel and Arons* [1960] model is an idealization of the interior flow in which a spatially uniform upwelling is assumed at the base of the thermocline. Deep water is assumed to flow northward away from the circumpolar region as a barotropic western boundary current. Water from the boundary current is fed into the interior uniformly at all levels such that the upwelling rate increases uniformly upward, i.e., dw/dz is constant. Geostrophy and mass conservation constrain the interior flow. *Fiadeiro* [1982] produced a radiocarbon simulation for the deep Pacific using a variation of the Stommel and Arons abyssal circulation model. In Fiadeiro's model the GEOSECS radiocarbon observations are used to fix the model concentrations at 1 km, its upper boundary. Fiadeiro found that the ^{14}C minimum in the North Pacific could not be reproduced by the Stommel and Arons flow field in its pure form. Instead, dw/dz must change sign in the interior such that mid-depth water flows to the south. Fiadeiro took this requirement to be a reflection of baroclinicity in the real ocean in which the deep interior flow is uncoupled from the upper ocean flow by the thermal structure, as described by *Wyrtki* [1961]. This finding is entirely consistent with the flow field produced by the GFDL model.

Maier-Reimer and Hasselmann [1987] have produced a global radiocarbon simulation using the dynamical ocean model described by *Hasselmann* [1982]. The model follows the quasi-geostrophic approximations and uses distinct fric-

tional layers at the equator and near continental margins where a geostrophic balance is not obtained. It runs about 10–20 times faster than the GFDL primitive equation model with the same resolution. The Maier-Reimer and Hasselmann model, hereinafter referred to as the Hamburg model, treats ^{14}C concentrations explicitly and computes $^{14}C/^{12}C$ ratios using a separate tracer field for ^{12}C. It can also be run using simulated particle fluxes, which transport carbon to depth independently of the circulation.

The radiocarbon simulations of Maier-Reimer and Hasselmann show distinct differences from those in this paper, reflecting significant differences in the circulation. The first thing one notices in comparing the P simulation with the abiotic version of the Hamburg model is the generally younger water in the North Pacific ^{14}C minimum in the Hamburg model. This is readily accounted for when one compares predicted ^{14}C values adjacent to Antarctica (-80 to $-100‰$ in the Hamburg model versus $-160‰$ in P and -140 to $-160‰$ in the observations).

The vertical overturning in the Hamburg model is redrawn here as Figure 20. The most significant differences can be seen in the high latitudes of the southern hemisphere. The circumpolar overturning cell penetrates below 3500 m in the GFDL model but is less than 1000 m deep in the Hamburg model. Downward flow in mid-latitudes moves poleward between 1 and 2 km, beneath the shallow circumpolar cell. It sinks again in the Antarctic, where it becomes part of the abyssal circulation. Consequently, radiocarbon ages adjacent to Antarctica in the Hamburg model are much too young.

As we discussed previously, poleward flows across the latitude belt of the Drake Passage are inhibited in the GFDL model above the depth of the sill connecting South America and Antarctica. We do not know why our circulation differs so much from that of the Hamburg model. The answer may involve something as simple as the Drake Passage bathymetry or something more fundamental, like a different dynamic balance in the circumpolar gap.

Another noteworthy difference between the two models can be seen in the tropics. Flow lines from the abyssal circulation in the Hamburg model pass up through the thermocline and join up with the shallow, wind-driven
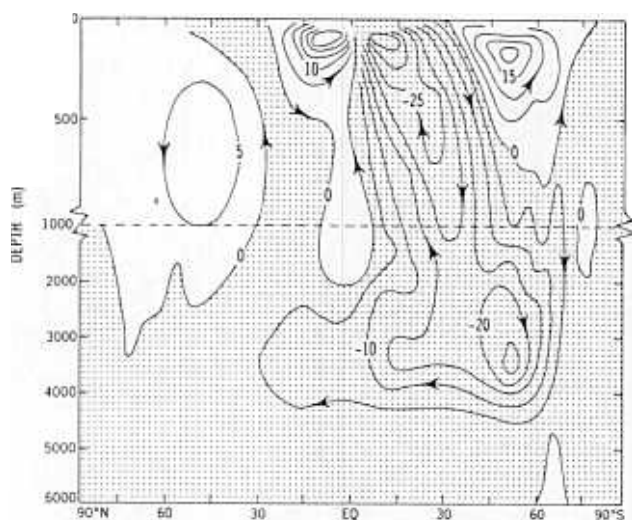
Fig. 20. Meridional transport stream function, zonally integrated, from the ocean general circulation model of *Maier-Reimer and Hasselmann* [1987]. Maier-Reimer and Hasselmann's Figure 6 has been redrawn here to correspond to the north-south and depth scale conventions of Figure 4 in this paper.

equatorial cell. Flow lines through the equatorial region in the GFDL model are closed within the upper kilometer. Our abyssal circulation is thus far more layered. K. Hasselmann (personal communication, 1988) has informed us that the Hamburg model's radiocarbon values at the surface in the eastern tropical Pacific are much too old.

CONCLUSIONS

In some respects, radiocarbon is like many other ocean tracers. Its sources and sinks are widely distributed, leaving its interior distributions with large-scale features that do not differentiate processes of advection from a large background of mixing. In several other respects, radiocarbon is a unique oceanographic tracer. Like temperature, its main gradient spans a vertical range extending from surface water into the deep sea; mixing across the thermocline represents an important process in its interior balance. Unlike temperature, its surface values are only weakly controlled by the atmosphere. This property makes its surface values an interpretable quantity, sensitive to how the interior balance is maintained. Like silica, the most differentiated radiocarbon concentrations in the ocean are found in the poorly ventilated waters of the deep Pacific. Decay of ^{14}C lowers radiocarbon values much as silica dissolution from bottom sediments increases concentrations of silica. The "old water" signal from radiocarbon decay is stronger, however, setting up a more clear Pacific-Antarctic contrast than is evident in the silica distribution.

We have used these properties of radiocarbon to examine the GFDL coarse-resolution ocean model's ability to ventilate its deep interior spaces. With the exception of a few notable deficiencies, the model successfully reproduces the important large-scale features of the radiocarbon distribution. We have also examined the circulation produced by a semidiagnostic model in which interior temperatures and salinities are restored toward observed values. Somewhat paradoxically, the basic prognostic version of the model, the version in which interior temperature and salinity fields deviate noticeably from observed values, produces a clearly

superior circulation, as deduced from its more real-looking radiocarbon predictions. We have found that the restoring terms in the diagnostic model suppress advective and convective motions in several important areas as they attempt to force the model circulation away from its preferred state. The fact that the prognostic model produces a better simulation than the diagnostic model does not mean that the prognostic model could not produce an even better simulation if it were also capable of producing more realistic temperature and salinity fields; the general success of the prognostic model does suggest, however, that the deviant temperature and salinity fields in themselves do not seriously degrade the interior ventilation.

The most important ingredients of the model's success are a moderately low, but still significant, value of 0.3 cm^2 s^{-1} for the coefficient of vertical diffusion in the upper kilometer and the model's realization of the ventilation in the circumpolar and Antarctic regions. Analysis of the global balance of ^{14}C between atmospheric inputs, decay, and redistribution by transport shows that between 35°S and 35°N about two thirds of the decay of ^{14}C over the water column is balanced by local inputs of ^{14}C from the atmosphere, which must be transported across the thermocline by vertical mixing. Larger vertical diffusion rates of order 1.0 cm^2 s^{-1} grossly distort deep-sea distributions of ^{14}C, while smaller values would produce prebomb surface concentrations too close to atmospheric equilibrium. We have found that spatial differences in gas exchange rates at the sea surface have a negligible effect on deepwater radiocarbon values.

The model ventilates its circumpolar region by a deep overturning cell which in turn controls the ventilation of the deep Pacific and Indian Ocean basins. There is relatively little flow of Pacific and Indian deep water southward across this latitude belt as envisioned in the classical oceanographic writings of Deacon and Sverdrup. The resistance to exchange across 50°–60°S defines much of the ^{14}C structure predicted by the model in the deep ocean basins.

The most significant shortcomings of the model are its failure to form proper intermediate water (a subject taken up in part 2) and failure to form North Atlantic Deep Water which is dense enough to fill the North Atlantic basin. A bottom layer almost 2000 m thick of Antarctic origin is allowed to penetrate to the northern extremes of the Atlantic basin. It is not clear how a denser NADW would affect the interior ventilation. This subject is currently under study.

Although the model produces very reasonable-looking simulations of the radiocarbon distribution in the deep sea, this does not prove that the mechanisms produced by the model are entirely accurate. The best test of the model predictions would be more detailed comparisons of the predictions and the observations. Unfortunately, this is not possible with the GEOSECS data set. With the exception of the Indian Ocean, the GEOSECS sections give a very limited view of the three-dimensional structure. While downwelling along the northern edge of the circumpolar current can be broadly inferred from the GEOSECS data, many other important predicted features of the circumpolar cell, like the southward flow under the current in layer 11 (Figure 19) cannot be resolved. Other tracers may not resolve this flow because Pacific-Antarctic contrasts are not as large as those of ^{14}C. In upcoming sampling expeditions, more attention needs to be paid to resolving ^{14}C differences within

deep-sea frontal regions and adjacent to north-south trending ridges and ocean margins.

REFERENCES

Alexander, R. C., and R. L. Mobley. Monthly average sea surface temperatures and ice pack limits on a 1° global grid, *Mon. Weather Rev.*, *104*, 143–148, 1976.

Broecker, W. S., A revised estimate for the radiocarbon age of North Atlantic deep water, *J. Geophys. Res.*, *84*, 3218–3226, 1979.

Broecker, W. S., and T.-H. Peng. Gas exchange rates between air and sea, *Tellus*, *26*, 21–35, 1974.

Broecker, W. S., and T.-H. Peng, *Tracers in the Sea*, Lamont-Doherty Geological Observatory, Palisades, N. Y., 1982.

Broecker, W. S., T.-H. Peng, H. G. Ostlund, and M. Stuiver. The distribution of bomb radiocarbon in the ocean. *J. Geophys. Res.*, *90*, 6953–6970, 1985a.

Broecker, W. S., T. Takahashi, and T. Takahashi. Sources and flow patterns of deep-ocean waters as deduced from potential temperature, salinity, and initial phosphate concentration. *J. Geophys. Res.*, *90*, 6925–6939, 1985b.

Bryan, F., Parameter sensitivity of primitive equation ocean general circulation models, *J. Phys. Oceanogr.*, *17*, 970–985, 1987.

Bryan, K., A numerical method for the study of the circulation of the world ocean, *J. Comput. Phys.*, *4*(3), 347–376, 1969.

Bryan, K., Models of the world ocean, *Dyn. Atmos. Oceans*, *3*, 327–338, 1979.

Bryan, K., Accelerating the convergence to equilibrium of ocean climate models, *J. Phys. Oceanogr.*, *14*, 666–673, 1984.

Bryan, K., and M. D. Cox, An approximate equation of state for numerical models of the ocean circulation, *J. Phys. Oceanogr.*, *2*, 510–514, 1972.

Bryan, K., and L. J. Lewis, A water mass model of the world ocean circulation, *J. Geophys. Res.*, *84*, 2503–2517, 1979.

Deacon, G. E. R., Note on the dynamics of the southern ocean, *Discovery Rep.*, *15*, 125–152, 1937.

Druffel, E. M., Radiocarbon in annual coral rings from the eastern tropical Pacific Ocean, *Geophys. Res. Lett.*, *8*, 59–62, 1981.

Druffel, E. R. M., Bomb radiocarbon in the Pacific: Annual and seasonal timescale variations, *J. Mar. Res.*, *45*, 667–698, 1987.

Druffel, E. R. M., Variability of ventilation in the North Atlantic determined from high precision measurements of bomb radiocarbon in banded corals, *J. Geophys. Res.*, *94*, 3271–3285, 1989.

Druffel, E. M., and H. E. Suess, On the radiocarbon record in banded corals: Exchange parameters and net transport of $^{14}CO_2$ between atmosphere and surface ocean, *J. Geophys. Res.*, *88*, 1271–1280, 1983.

Esbensen, S. K., and Y. Kushnir, The heat budget of the global ocean: An atlas based on estimates from surface marine observations, *Rep. 29, Clim. Res. Inst.*, Oreg. State Univ., Corvallis, 1981.

Fiadeiro, M. E., Three-dimensional modeling of tracers in the deep Pacific Ocean, II, Radiocarbon and the circulation, *J. Mar. Res.*, *40*, 537–550, 1982.

Fine, R. A., Direct evidence using tritium data for through flow from the Pacific into the Indian Ocean, *Nature*, *315*, 478–480, 1985.

Gill, A. E., and K. Bryan, Effects of geometry on the circulation of a three-dimensional southern-hemisphere ocean model, *Deep Sea Res.*, *18*, 685–721, 1971.

Gordon, A. L., General ocean circulation, in *Numerical Models of*

the *Ocean Circulation*, pp. 39–53, National Academy of Sciences, Washington, D. C., 1975.

Hasselmann, K., An ocean model for climate variability studies, *Prog. Oceanogr.*, *11*, 69–92, 1982.

Hellerman, S., and M. Rosenstein, Normal monthly wind stress over the world ocean with error estimates, *J. Phys. Oceanogr.*, *13*, 1093–1104, 1983.

Knauss, J., A note on the transport of the Gulf Stream, *Deep Sea Res.*, *16*, suppl., 117–124, 1969.

Konishi, K., T. Tanaka, and M. Sakanoue, Secular variation of radiocarbon concentration in sea water: Sclerochronological approach, in *Proceedings of the Fourth International Coral Reef Symposium, Manila*, vol. 1, edited by E. D. Gomez, pp. 181–185, Marine Science Center, University of the Philippines, 1982.

Levitus, S., Climatological Atlas of the World Ocean, *NOAA Prof. Pap. 13*, U.S. Government Printing Office, Washington, D. C., 1982.

Maier-Reimer, E., and K. Hasselmann, Transport and storage of CO_2 in the ocean—An inorganic ocean circulation carbon cycle model, *Clim. Dyn.*, *2*, 63–90, 1987.

Manabe, S., and R. J. Stouffer, Two stable equilibria of a coupled ocean-atmosphere model. *J. Clim.*, *1*, 841–866, 1988.

McCartney, M. S., Subantarctic mode water, in *A Voyage of Discovery*, edited by M. Angel, pp. 103–119, Pergamon, Elmsford, N. Y., 1977.

McCartney, M. S., The subtropical recirculation of mode waters, *J. Mar. Res.*, *40*, suppl., 427–464, 1982.

Nozaki, Y., D. M. Rye, K. K. Turekian, and R. E. Dodge, A 200 year record of carbon-13 and carbon-14 variations in Bermuda coral, *Geophys. Res. Lett.*, *5*, 825–828, 1978.

Oeschger, H., H. Siegenthaler, U. Schotterer, and A. Gugelmann, A box-diffusion model to study the carbon dioxide exchange in nature, *Tellus*, *27*, 168–192, 1975.

Ostlund, H. G., and M. Stuiver, GEOSECS Pacific radiocarbon, *Radiocarbon*, *22*, 25–53, 1980.

Philander, S. G. H., W. J. Hurlin, and A. D. Seigel, Simulation of the seasonal cycle of the tropical Pacific Ocean, *J. Phys. Oceanogr.*, *17*, 1986–2002, 1987.

Piola, A. R., and A. L. Gordon, Pacific and Indian Ocean upper-layer salinity budget, *J. Phys. Oceanogr.*, *14*, 747–753, 1984.

Reid, J. L., On the contribution of the Mediterranean Sea outflow to the Norwegian-Greenland Sea, *Deep Sea Res.*, *26*, 1199–1223, 1979.

Reid, J. L., On the mid-depth circulation of the world ocean, in *Evolution of Physical Oceanography*, edited by B. A. Warren and C. Wunsch, pp. 70–111, MIT Press, Cambridge, Mass., 1981.

Roemmich, D., and C. Wunsch, Two trans-atlantic sections: Meridional circulation and heat flux in the subtropical North Atlantic Ocean, *Deep Sea Res.*, *32*, 619–664, 1985.

Sarmiento, J. L., On the north and tropical Atlantic heat balance, *J. Geophys. Res.*, *91*, 11,677–11,698, 1986.

Sarmiento, J. L., and K. Bryan, An ocean transport model for the North Atlantic, *J. Geophys. Res.*, *87*, 394–408, 1982.

Stommel, H., and A. B. Arons, On the abyssal circulation of the world ocean, II, An idealized model of the circulation pattern and amplitude in oceanic basins, *Deep Sea Res.*, *6*, 217–233, 1960.

Stuiver, M., and H. G. Ostlund, GEOSECS Atlantic radiocarbon, *Radiocarbon*, *22*, 1–24, 1980.

Stuiver, M., and H. G. Ostlund, GEOSECS Indian Ocean and Mediterranean radiocarbon, *Radiocarbon*, *25*, 1–29, 1983.

Stuvier, M., and H. A. Polach, Discussion: Reporting of ^{14}C data, *Radiocarbon*, *19*, 355–363, 1977.

Stuiver, M., P. D. Quay, and H. G. Ostlund, Abyssal water carbon-14 distribution and the age of the world oceans, *Science*, *219*, 849–851, 1983.

Sverdrup, H. U., M. W. Johnson, and R. H. Fleming, *The Oceans*, 1087 pp., Prentice Hall, Englewood Cliffs, N. J., 1942.

Toggweiler, J. R., A six zone regionalized model for bomb radiotracers and CO_2 in the upper kilometer of the Pacific Ocean, Ph.D. thesis, Columbia Univ., New York, 1983.

Toggweiler, J. R., K. Dixon, and K. Bryan, Simulations of radiocarbon in a coarse-resolution world ocean model, 2, Distributions of bomb-produced carbon 14, *J. Geophys. Res.*, this issue.

Veronis, G., The role of models in tracer studies, in *Numerical Models of Ocean Circulation*, pp. 133–146, National Academy of Sciences, Washington, D. C., 1975.

Warren, B. A., General circulation of the South Pacific, in *Scientific Exploration of the South Pacific*, edited by W. Wooster, pp. 33–49, National Academy of Sciences, Washington, D. C., 1970.

Warren, B. A., Deep circulation of the world ocean, in *Evolution of Physical Oceanography*, edited by B. A. Warren and C. Wunsch, pp. 6–40, MIT Press, Cambridge, Mass., 1981.

Whitworth, T., III, and R. G. Peterson, Volume transport of the Antarctic Circumpolar Current from bottom pressure measurements, *J. Phys. Oceanogr., 15*, 810–816, 1985.

Whitworth, T., III, W. D. Nowlin, and S. J. Worley, The net transport of the Antarctic Circumpolar Current through Drake Passage, *J. Phys. Oceanogr., 12*, 960–971, 1982.

Wunsch, C., D.-X. Hu, and B. Grant, Mass, heat, salt, and nutrient fluxes in the South Pacific Ocean, *J. Phys. Oceanogr., 13*, 725–753, 1983.

Wyrtki, K., The thermohaline circulation in relation to the general circulation in the oceans, *Deep Sea Res., 8*, 39–64, 1961.

K. Bryan, K. Dixon, and J. R. Toggweiler, Geophysical Fluid Dynamics Laboratory, NOAA, Princeton University, Princeton, NJ 08542.